Cramér-Rao Bound Optimization for Multi-Functional Surface-Aided ISAC Systems

Runlong Ye, *Graduate Student Member, IEEE*, Yuyang Peng, *Senior Member, IEEE*, Ming Yue, Wei Gan, Fawaz Al-Hazemi, *Senior Member, IEEE*, Juho Lee, *Fellow, IEEE*, and Raouf Boutaba, *Fellow, IEEE*

***Abstract*—In this work, we propose the deployment of a multi-functional surface (MFS) with both coupled and independent phase-shift architectures to support integrated sensing and communication (ISAC) networks. Specifically, the MFS is divided into two functional components: an amplify-then-transmit-and-reflect part and a sensing part, which together help to mitigate the multi-fading effect (MFE), enable full-angle coverage, and facilitate target sensing. We first derive a closed-form expression for the Cramér-Rao bound (CRB) associated with two-dimensional angle-of-arrival (AoA) estimation assisted by the MFS. We then formulate CRB minimization problems under various practical constraints for both coupled and independent phase-shift configurations. To address the non-convex nature and complexity of the resulting optimization problems, we introduce several efficient solution strategies. In particular, we employ penalty dual decomposition (PDD) and block coordinate descent (BCD) methods to decouple the optimization variables. For the coupled phase-shift case, we further derive closed-form solutions for subproblems introduced by the PDD framework. Numerical and simulation results confirm that the proposed scheme achieves a significantly lower root CRB compared to baseline approaches, especially when amplifiers are integrated into the MFS and the more practical independent phase-shift design, despite its higher manufacturing cost, is considered.**

***Index Terms*—Integrated sensing and communication, multi-functional surface, Cramér-Rao bound, coupled phase-shift, independent phase-shift.**

Received 24 August 2025; revised 1 February 2026 and 7 May 2026; accepted 19 June 2026. Date of publication 7 July 2026; date of current version 10 July 2026. This work was supported in part by the Science and Technology Development Fund, Macau SAR (0085/2024/RIA2) and in part by Research Fund of Dongguan Polytechnic (2025a02). The associate editor coordinating the review of this article and approving it for publication was A.-A. A. Boulogeorgos. *(Corresponding author: Yuyang Peng.)*

Runlong Ye, Yuyang Peng, and Ming Yue are with the School of Computer Science and Engineering, Macau University of Science and Technology, Macau, China (e-mail: 3220002479@student.must.edu.mo; yypeng@must.edu.mo; 3230002258@student.must.edu.mo).

Wei Gan is with the School of Computer Science and Engineering, Macau University of Science and Technology, Macau, China, and also with Dongguan Polytechnic, Dongguan, Guangdong 523808, China (e-mail: 2202853gii30001@student.must.edu.mo).

Fawaz Al-Hazemi is with the Department of Computer and Network Engineering, University of Jeddah, Jeddah 21959, Saudi Arabia (e-mail: fmalhazemi@uj.edu.sa).

Juho Lee is with Samsung Research, Samsung Electronics, Seoul 06765, South Korea (e-mail: juho95.lee@samsung.com).

Raouf Boutaba is with the David R. Cheriton School of Computer Science, University of Waterloo, Waterloo, ON N2L 3G1, Canada (e-mail: rboutaba@uwaterloo.ca).

Digital Object Identifier 10.1109/TWC.2026.3707963

I. Introduction

As ONE of the key technologies for sixth-generation (6G) communication, integrated sensing and communication (ISAC) is expected to address the issue of spectrum congestion caused by the separate allocation of resources for sensing and communication. In particular, base stations (BSs) and radars are traditionally used for wireless communication and sensing, respectively. However, deploying separate hardware for each function incurs high equipment costs. Additionally, both functions compete for limited spectrum resources, making spectrum efficiency increasingly critical. Given the similarity in signal processing techniques for communication and sensing [1], it is natural to integrate them into a shared hardware platform. To realize this integration, [2] proposed a branch-and-bound algorithm to obtain a globally optimal waveform design for multiple-input multiple-output (MIMO) dual-functional radar-communication (DFRC) systems. Numerical results showed that communication performance could be significantly improved with only a slight degradation in radar performance. Further, [3] introduced a Cramér-Rao bound (CRB) minimization problem for both point and extended targets for the first time, demonstrating that CRB serves as a reliable performance metric for sensing.

However, when users or targets are located in unfavorable propagation environments, such as when direct paths are blocked by obstacles, sensing and communication performance can degrade significantly. To overcome this, [4], [5], [6] proposed the use of reconfigurable intelligent surfaces (RISs) to equip multiple controllable reflective elements [7]. These can reroute signals around obstacles by optimizing passive beamforming. Due to the half-space coverage limitation of traditional RISs, [8] and [9] proposed the simultaneously transmitting and reflecting RIS (STAR-RIS) to achieve full-space coverage. This is particularly suitable for ISAC applications where users and targets may be located on opposite sides of the RIS. Hence, deploying STAR-RIS in ISAC systems can improve both communication and sensing performance [10], [11], [12].

From both communication and sensing perspectives, however, STAR-RIS systems can suffer from severe path loss due to the multiplicative fading effect (MFE) in the BS→RIS→user and BS→RIS→target→RIS→BS links. To mitigate this, [10], [11] proposed adding sensors to STAR-RIS forming a simultaneously transmitting and reflecting surface (STARS). In this configuration, the sensing task is offloaded to the embedded sensors, thereby shortening the sensing link to BS $\rightarrow$ RIS $\rightarrow$ target $\rightarrow$ RIS, effectively reducing the MFE.

Alternatively, the MFE can be addressed by equipping STAR-RIS with amplifiers, resulting in what is known as an active STAR-RIS [13]. This design offers both MFE mitigation and full-space coverage, improving the capabilities of both traditional STAR-RIS [9] and active RIS [14]. As an application of active STAR-RIS in ISAC, [15] investigated a joint optimization framework that maximizes the sum rate of users while satisfying signal-to-interference-plus-noise ratio (SINR) constraints for targets. Their results confirm that active STAR-RIS outperforms STAR-RIS, active RIS, and conventional RIS in sensing performance. To further mitigate the MFE, [16] proposed integrating sensors into active STAR-RIS, creating a multi-functional surface (MFS) for ISAC. This configuration not only eliminates one hop (the RIS$\rightarrow$BS link) in the echo sensing path but also amplifies both transmitted and reflected signals. Despite this advancement, the general sensing performance metric, CRB, has not yet been considered in the context of MFS-assisted ISAC systems. CRB, which quantifies the lower bound on mean squared error (MSE) for unbiased estimators [3], is a fundamental benchmark for evaluating sensing performance. However, due to the amplifiers introduced in MFS, active RIS, and active STAR-RIS, the dynamic noise generated complicates the CRB analysis. In [17], the authors studied CRB for one-dimensional (1D) angle-of-arrival (AoA) estimation using a uniform linear array (ULA)-based active RIS, incorporating the effect of dynamic noise. The CRB analysis for amplifier- and sensor-assisted uniform planar array (UPA)-based MFS has not been explored. Consequently, the explicit optimization of CRB as a system-level performance metric remains an open challenge. Furthermore, according to the active STAR-RIS architecture in [13], the use of a 90° hybrid coupler is crucial to minimize power loss for the incident signal. This architectural choice leads to lower manufacturing costs for coupled phase-shift designs and higher costs for independent phase-shift designs. Despite these implications, the impact of phase-shift architecture on beamforming design in MFS/active STAR-RIS-assisted ISAC systems has not been fully investigated.

Motivated by the above, in this work, we investigate the minimization of the CRB in an MFS-aided ISAC system, considering both coupled and independent phase-shift architectures. Our focus is on two-dimensional (2D) AoA estimation at the MFS. The main contributions of this work are summarized as follows:

1) We propose an MFS-based ISAC framework, where the MFS comprises amplify-then-transmit-and-reflect (A&T&R) elements and embedded sensors. This hybrid structure enables both mitigation of the MFE and full-space coverage. Furthermore, we account for two hardware configurations: coupled phase-shift, which is cost-effective, and independent phase-shift, which provides more flexibility at the expense of higher manufacturing costs. Our scheme accommodates both configurations in the system design.

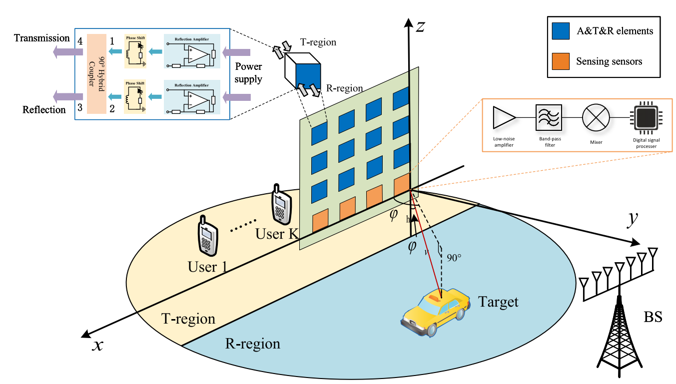

Fig. 1. Illustration of ISAC system assisted by an MFS.

2) We derive a closed-form expression for the CRB corresponding to 2D AoA estimation in the proposed MFS-aided ISAC system. This CRB quantifies the theoretical lower bound of the MSE for target localization. The derivation is significantly more involved than in passive RIS cases due to the presence of amplifiers, which introduce dynamic noise.
3) Based on the derived closed-form CRB, we formulate CRB minimization problems for both coupled and independent phase-shift configurations, subject to various practical system constraints. To address the challenges posed by highly coupled optimization variables, which result in the non-convexity of the formulated problems, we develop solution frameworks based on penalty dual decomposition (PDD) and block coordinate descent (BCD). In particular, to decouple the coupled phase-shift constraints, we introduce auxiliary variables, which transform the problem into a more tractable subproblem. We then derive a closed-form solution for this subproblem, enabling efficient optimization while preserving the structure of the original problem.
4) Numerical and simulation results demonstrate that the root CRB achieved by the proposed scheme is significantly lower than that of existing approaches, particularly when amplifiers are integrated into the MFS and the realistic independent phase-shift configuration, despite its higher manufacturing cost, is employed.

Organization: The remainder of the paper is structured as follows. Section II presents the system model of the proposed scheme and formulates the CRB minimization problems. Section III reformulates the original problems into more tractable forms, highlighting the associated challenges and the methods developed to address them. Sections IV and V describe efficient solution techniques for the resulting problems under the coupled and independent phase-shift cases, respectively, as outlined in Section III. Section VI provides simulation results, comparing the performance of the proposed scheme with various baselines in terms of root CRB. Finally, Section VII concludes the paper.

II. System Model and Problem Formulation

In this work, we assume that the direct links between the BS and the users, as well as between the BS and the target, are blocked. To address this, we introduce an MFS into the ISAC system to provide both communication and sensing services. The MFS thereby enables full-space coverage and helps mitigate the MFE. The system model is illustrated in Fig. 1. Specifically, we consider a BS equipped with N_t antennas and an MFS comprising $N_{\text{tot}} = N + N_s$ elements, where N and N_s denote the numbers of A&T&R elements and sensing elements, respectively. The network also includes a target and K single-antenna users. For simplicity and without loss of generality, we assume that the users are located in the transmission region (T-region) and the target in the reflection region (R-region). The MFS is logically divided into two parts: the A&T&R elements, which amplify and simultaneously transmit and reflect the incoming signals, and the sensors, which are used to detect and localize the target. The BS and the MFS are assumed to be connected via a dedicated link to facilitate information exchange. Based on these two functional roles of the MFS, the surface can simultaneously support both communication and sensing services. Specifically, communication is enabled via the BS $\rightarrow$ MFS $\rightarrow$ user link, while sensing is performed through the BS $\rightarrow$ MFS $\rightarrow$ target $\rightarrow$ sensor link. Let $\mathbf{G} \in \mathbb{C}^{N\times N_t}$ denote the channel between the BS and the MFS, and $\boldsymbol{h}_k \in \mathbb{C}^{N\times 1}$ denote the channel between the MFS and the kth user. The channel between the MFS and the target will be detailed in II-D. We assume perfect channel state information (CSI) is available for $\mathbf{G}$ and $\boldsymbol{h}_k$, which can be obtained using state-of-the-art channel estimation techniques [18], [19].

A. Transmitted Signal

The BS sends precoded signals that integrate sensing and communication information for K users and the target, which is given by $X = [\boldsymbol{x}_1, \ldots, \boldsymbol{x}_L] = \mathbf{W}\mathbf{S}_{\text{C}} = \Big[\sum_{k=1}^{K} \boldsymbol{w}_k s_{1,k} + \sum_{a=K+1}^{K+N_t} \boldsymbol{w}_a s_{1,a}, \ldots, \sum_{k=1}^{K} \boldsymbol{w}_k s_{L,k} + \sum_{a=K+1}^{K+N_t} \boldsymbol{w}_a s_{L,a}\Big]$ with L denoting the total number of blocks for transmitting signals and $L > N_t$ [3], where $\mathbf{W} = [\boldsymbol{w}_1, \ldots, \boldsymbol{w}_K, \boldsymbol{w}_{K+1}, \ldots, \boldsymbol{w}_{K+N_t}] \in \mathbb{C}^{N_t\times(K+N_t)}$ denotes the precoding matrix, and $\mathbf{S}_{\text{C}} \in \mathbb{C}^{(K+N_t)\times L} = [\boldsymbol{s}_1, \ldots, \boldsymbol{s}_L]$ collects all signals with $\boldsymbol{s}_l = [s_{l,1}, \ldots, s_{l,K+N_t}]^T$. Note that $\sum_{k=1}^{K} \boldsymbol{w}_k s_{l,k}, \forall l \in \mathcal{L} \triangleq \{1, \ldots, L\}$ represents the precoded communication signals at the lth block intended for K users, while $\sum_{a=K+1}^{K+N_t} \boldsymbol{w}_a s_{l,a}, \forall l \in \mathcal{L}$ represents the dedicated sensing signals at the lth block intended for the target. Here, we generate independent Gaussian random signals for communication signals $\boldsymbol{s}_{l,k}, \forall k \in \mathcal{K} \triangleq \{1, \ldots, K\}$ and pseudo-random coding for sensing signals $\boldsymbol{s}_{l,a}, \forall a \in \mathcal{A} \triangleq \{K+1, \ldots, K+N_t\}$ [10], [20], and thus $\mathbb{E}\{s_{l,b}s_{l,b'}^*\} = 0, \forall b \neq b', \forall b \in \mathcal{B} \triangleq \{1, \ldots, K+N_t\}, b' \in \mathcal{B}$, and $\mathbb{E}\{s_{l,k}s_{l,k}^*\} = 1, \forall k \in \mathcal{K}$. In addition, by letting $\bar{\boldsymbol{x}}_l = \sum_{a=K+1}^{K+N_t} \boldsymbol{w}_a s_{l,a}, \forall l \in \mathcal{L}$ collecting all signals tended for the target at the lth duration time, we have $\mathbf{R}_s = \mathbb{E}\{\bar{\boldsymbol{x}}_l \bar{\boldsymbol{x}}_l^H\}$ representing the covariance matrix of the dedicated sensing signal. Then, by noting that $\frac{1}{L}\mathbf{S}_{\text{C}}\mathbf{S}_{\text{C}}^H = \mathbf{I}_K$ for sufficiently large L, the covariance matrix of the transmitted signal is expressed as $\mathbf{R}_x = \frac{1}{L}\mathbf{X}\mathbf{X}^H \approx \mathbf{W}\mathbf{W}^H = \sum_{k=1}^{K} \boldsymbol{w}_k \boldsymbol{w}_k^H + \mathbf{R}_s$. Due to the limited available power at the BS, the power of transmitted signal should satisfy the following constraint

$$\sum_{k=1}^{K} \boldsymbol{w}_k \boldsymbol{w}_k^H + \operatorname{Tr}(\mathbf{R}_s) = \operatorname{Tr}(\mathbf{R}_x) \leq P_{\text{BS}}^{\max}, \tag{1}$$

where $P_{\text{BS}}^{\max}$ denotes the maximum available power at the BS.

B. MFS Model

To further mitigate the MFE in both the BS $\rightarrow$ MFS $\rightarrow$ target $\rightarrow$ sensor and BS $\rightarrow$ MFS $\rightarrow$ user links within the ISAC system, amplifiers are introduced at the MFS, connected to the corresponding phase shifters, and a smart controller is employed to exchange information between the MFS and the BS. As illustrated in Fig. 1 [13], each element of the MFS is equipped with two amplifiers and two phase shifters: one amplifier and one phase shifter are associated with the transmitting path, and the other pair with the reflecting path. The amplifiers serve to boost the incoming signals for realizing reflection and transmission signals power. This amplification is achieved through power supply via the amplifier, enabling stronger signal re-radiation. In addition, as shown in Fig. 1, the left and right phase shifters control the transmission and reflection phase-shift, respectively, where a positive-intrinsic-negative (PIN) diode is embedded in each phase shifter, and the phase-shift can be adjusted by controlling its corresponding biasing voltage via a direct-current (DC) line [7]. This phase control allows precise steering of electromagnetic wavefronts. By programming the phase distribution across elements, the MFS can dynamically reconfigure spatial radiation patterns to optimize communication. Moreover, the 3-dB 90° hybrid coupler is used to couple incident signal from ports 1 and 2 to ports 3 and 4 as output signal, which can minimize power loss and thus avoiding the incoming power waste [13].[1] To proceed, we denote the region index $i \in \{t, r\}$, where t corresponds to the T-region and r to the R-region. The transmitting or reflecting phase shift matrix for region i is then defined as $\boldsymbol{\Theta}_i = \operatorname{Diag}(\underbrace{[\varrho_{i,1}e^{j\theta_{i,1}}, \ldots, \varrho_{i,N}e^{j\theta_{i,N}}]^T}_{\boldsymbol{v}_i})$ with $\theta_{i,n}$ and $\varrho_{i,n}, \forall i \in \{t, r\}, n \in \mathcal{N} \triangleq \{1, \ldots, N\}$ being the nth phase-shift and the corresponding amplitude of the nth phase shifter for i-region, respectively. According to [13], there are two cases of phase-shift configurations for realizing simultaneous transmission and reflection as described in the following subsections.

1) Coupled Phase-Shift: In this configuration, only one phase shifter and one amplifier are required to enable simultaneous transmission and reflection, which is practically realizable and thus reduces manufacturing costs. To further investigate the coupled phase-shift configuration, in Fig. 1, we

[1] In fact, the proposed surface may occur anomalous refraction, which may degrade the transmission of the MFS. To address this issue, the authors in [21] and [22] proposed surfaces with two-dimensional planar periodic metagrating and all-dielectric quasi-three-dimensional sub-wavelength structures, respectively, and the potential impact of the proposed scheme on it will be investigated along with the proposed MFS in our future work, as an assumption of perfect anomalous refraction can help us to explore the sensing performance upper bound of the proposed scenario, which could provide theoretical engineering guidelines.

first denote V_u^+ and V_u^- as input and output signal voltages of uth port, respectively, then the output and input signal voltages satisfy the following relationship according to the scattering matrix of the 90° hybrid [13]:

$$\begin{bmatrix} V_1^- \\ V_2^- \\ V_3^- \\ V_4^- \end{bmatrix} = -\frac{\sqrt{2}}{2} \begin{bmatrix} 0 & 0 & 1 & j \\ 0 & 0 & j & 1 \\ 1 & j & 0 & 0 \\ j & 1 & 0 & 0 \end{bmatrix} \begin{bmatrix} V_1^+ \\ V_2^+ \\ V_3^+ \\ V_4^+ \end{bmatrix}, \tag{2}$$

where the coefficient $-\frac{\sqrt{2}}{2}$ in (2) means that the 90° coupler divides input power equally, with each output port receiving half the input power (a 3-dB reduction). In this coupled phase-shift structure, the output voltages at ports 3 and 4 are respectively given in the following according to (2)

$$\begin{aligned} V_3^- &= -\frac{\sqrt{2}}{2}\left(V_1^+ + jV_2^+\right), \\ V_4^- &= -\frac{\sqrt{2}}{2}\left(jV_1^+ + V_2^+\right). \end{aligned} \tag{3}$$

Since only one phase shifter and one amplifier at each element of the MFS are required to enable simultaneous transmission and reflection in the coupled phase-shift structure, if the port 1 is available and the port 2 is grounded, we have $V_1^+ = G_1 V_1^-$ and $V_2^+ = 0$, where G_1 represents the corresponding complex-valued gain including amplitude and phase-shift, and thus (3) becomes

$$\begin{aligned} V_3^- &= -\frac{\sqrt{2}}{2} G_1 V_1^-, \\ V_4^- &= -\frac{\sqrt{2}}{2} jG_1 V_1^-. \end{aligned} \tag{4}$$

Utilizing (2) again, we substitute $V_1^- = -\frac{\sqrt{2}}{2}(V_3^+ + jV_4^+)$ into (4), which yields

$$\begin{aligned} V_3^- &= \frac{1}{2} G_1 \left(V_3^+ + jV_4^+\right), \\ V_4^- &= \frac{1}{2} G_1 \left(jV_3^+ - V_4^+\right). \end{aligned} \tag{5}$$

As a result, the T&R coefficients, $\theta_{i,n}^R$ and $\theta_{i,n}^T, \forall i, n$, can be derived as:

$$\begin{aligned} \theta_{r,n}^R &= \left.\frac{V_3^-}{V_3^+}\right|_{V_4^+=0} = \frac{1}{2} G_1,\ \theta_{r,n}^T = \left.\frac{V_4^-}{V_4^+}\right|_{V_3^+=0} = -\frac{1}{2} G_1, \\ \theta_{t,n}^R &= \left.\frac{V_4^-}{V_3^+}\right|_{V_4^+=0} = \frac{1}{2} jG_1,\ \theta_{t,n}^T = \left.\frac{V_3^-}{V_4^+}\right|_{V_3^+=0} = \frac{1}{2} jG_1, \end{aligned} \tag{6}$$

where the superscripts, R and T, in (6) denote the region that the signal input. It can be observed from (6) that $\angle\theta_{r,n}^R - \angle\theta_{t,n}^R = -\pi/2$ and $\angle\theta_{r,n}^T - \angle\theta_{t,n}^T = \pi/2$, which implies that the difference between the reflection phase-shift and transmission phase-shift is $\pi/2$, and thus leading to the following coupled phase-shift constraints:

$$\begin{aligned} &\varrho_{r,n}^2 + \varrho_{t,n}^2 = 1, \quad \varrho_{i,n} \in [0,1], \quad \forall i, n, \\ &|\theta_{t,n} - \theta_{r,n}| = \frac{\pi}{2} \text{ or } \frac{3\pi}{2}, \quad \theta_{i,n} \in [0, 2\pi), \quad \forall i, n. \end{aligned} \tag{7}$$

2) Independent Phase-Shift: In this configuration, each MFS element requires two amplifiers and two phase shifters, which leads to higher manufacturing costs compared to the coupled phase-shift case. In this case, we have $V_1^+ = G_1 V_1^-$ and $V_2^+ = G_2 V_2^-$. Based on this, we substitute them into (3), which yields

$$\begin{aligned} V_3^- &= -\frac{\sqrt{2}}{2}\left(G_1 V_1^- + jG_2 V_2^-\right), \\ V_4^- &= -\frac{\sqrt{2}}{2}\left(jG_1 V_1^- + G_2 V_2^-\right). \end{aligned} \tag{8}$$

We substitute $V_1^- = -\frac{\sqrt{2}}{2}(V_3^+ + jV_4^+)$ and $V_2^- = -\frac{\sqrt{2}}{2}(jV_3^+ + V_4^+)$ obtained from (2) into (8), resulting in

$$\begin{aligned} V_3^- &= \frac{1}{2}\left(G_1 V_3^+ + jG_1 V_4^+ - G_2 V_3^+ + jG_2 V_4^+\right), \\ V_4^- &= \frac{1}{2}\left(jG_1 V_3^+ - G_1 V_4^+ + jG_2 V_3^+ + G_2 V_4^+\right). \end{aligned} \tag{9}$$

Following the same procedure as in (6), the T&R coefficients in the independent phase-shift case are derived as:

$$\begin{aligned} \theta_{r,n}^R &= -\theta_{r,n}^T = \left.\frac{V_3^-}{V_3^+}\right|_{V_4^+=0} = \frac{1}{2}\left(G_1 - G_2\right), \\ \theta_{t,n}^R &= \theta_{t,n}^T = \frac{1}{2} j\left(G_1 + G_2\right). \end{aligned} \tag{10}$$

It can be observed from (10) that, there is no explicit relationship between the reflection phase-shift and transmission phase-shift, so that they can be independently adjusted to achieve greater degrees of freedom (DoF) and higher performance improvement compared to the coupled phase-shift structure, as discussed in Sec. VI. This results in the following independent phase-shift constraints:

$$\begin{aligned} &\varrho_{r,n}^2 + \varrho_{t,n}^2 = 1, \quad \varrho_{i,n} \in [0,1], \quad \forall i, n, \\ &\theta_{i,n} \in [0, 2\pi), \quad \forall i, n. \end{aligned} \tag{11}$$

Therefore, when the coupled phase-shift and the independent phase-shift cases are considered, the amplification factor matrices can be denoted by $\mathbf{P}_i = \mathrm{Diag}([\sqrt{p_{i,1}}, \ldots, \sqrt{p_{i,N}}])$ and $\mathbf{P} = \mathrm{Diag}([\sqrt{p_1}, \ldots, \sqrt{p_N}])$, with $p_{i,n}, \forall i \in \{t, r\}, n \in \mathcal{N}$ representing the nth amplification factor for i-region and $p_n, \forall n \in \mathcal{N}$ representing the nth amplification factor, respectively. For simplicity and consistency, we denote the beamforming matrix at the MFS as $\boldsymbol{\Phi}_i, \forall i$, which is a diagonal matrix with each diagonal entry characterizing the amplitudes and phase-shift caused by amplifiers and phase shifters at the MFS, respectively, without violating (7) and (11) for the coupled phase-shift and the independent phase-shift cases, respectively. Specifically, due to the limited available power at the MFS, the set of beamforming matrices $\{\boldsymbol{\Phi}_i\}$ must satisfy the following non-negativity constraint:[2]

$$[\mathbf{\Phi}_i]_{n,n} \in [0, P_{\mathrm{A}}^{\max}], \quad \forall i, n. \tag{12}$$

Here, $P_{\mathrm{A}}^{\max}$ denotes the maximum available power at each amplifier of the MFS. It is important to note that the inclusion of amplifiers, which are used to boost incoming signals at the MFS, also results in the amplification of dynamic noise. As a result, the power of this amplified noise cannot be neglected [13], [14]. Accordingly, the MFS is subject to the following total power constraint:

$$\sum_{k=1}^{K}\left(\|\mathbf{\Phi}_t\mathbf{G}\boldsymbol{w}_k\|^2+\|\mathbf{\Phi}_r\mathbf{G}\boldsymbol{w}_k\|^2\right)+\sigma_{\mathrm{I}}^2\left(\|\mathbf{\Phi}_t\|_{\mathrm{F}}^2+\|\mathbf{\Phi}_r\|_{\mathrm{F}}^2\right)$$
$$+\operatorname{Tr}\left(\mathbf{\Phi}_t\mathbf{G}\mathbf{R}_s\mathbf{G}^H\mathbf{\Phi}_t^H+\mathbf{\Phi}_r\mathbf{G}\mathbf{R}_s\mathbf{G}^H\mathbf{\Phi}_r^H\right)\le P_{\mathrm{R}}^{\max}, \tag{13}$$

where $P_{\mathrm{R}}^{\max}$ represents the maximum available power at the MFS.

Remark 1: In fact, "A&T&R" means the arrangement sequence of circuit of the element, and the MFS is quiet different from the amplify-and-forward (AF) relay. Specifically, for the proposed scenario with the help of an MFS, the signal is first transmitted by the BS, and then be directly reflected and transmitted after colliding with the elements, without reception and being processed at the elements. In other words, because the MFS operates in full-duplex mode, the signal transmission of the BS and the reflection and transmission of the MFS are synchronized, requiring only one time slot instead of two as in AF-assisted wireless networks. Furthermore, compared to wireless communications assisted by MFS without RF chain, AF relay equipped with RF chain lacks the capability to reconfigure electromagnetic waves due to the absent of low-cost phase adjustment circuit [25], [26].

C. Received Signals at Users

Based on the above, the received signal at the kth user is given by[3]

$$\boldsymbol{y}_k^T=\boldsymbol{h}_k^H\mathbf{\Phi}_t\mathbf{G}\mathbf{X}+\boldsymbol{h}_k^H\mathbf{\Phi}_t\underbrace{\left[\boldsymbol{n}_{\mathrm{I}}^1,\ldots,\boldsymbol{n}_{\mathrm{I}}^L\right]}_{\mathbf{N}_{\mathrm{I}}}+\underbrace{\left[n_k^l,\ldots,n_k^L\right]}_{\boldsymbol{n}_{\mathrm{u}}^T}, \tag{14}$$

where the received signals are stacked over L duration time such that $\boldsymbol{y}_k^T=\left[y_k^1,\ldots,y_k^L\right]$; $\boldsymbol{n}_{\mathrm{I}}^l\sim\mathcal{CN}\left(\mathbf{0},\sigma_{\mathrm{I}}^2\mathbf{I}_N\right)$ represents the non-negligible dynamic noise at the MFS [14],[4] while $n_k^l\sim\mathcal{CN}\left(0,\sigma_u^2\right)$ represents the additive white Gaussian noise (AWGN) received at the users. Thus, the SINR of kth user is expressed in (15), shown at the bottom of the page.

D. Sensing Model

1) Received Signal at the MFS: Let the round-trip sensing channel be $\tilde{\mathbf{H}}=\alpha\mathbf{H}$ with $\mathbf{H}=\bar{\boldsymbol{h}}_r\boldsymbol{h}_r^T$, where α denotes the complex-valued channel coefficient [3], and $\boldsymbol{h}_r\in\mathbb{C}^{N\times 1}$ and $\bar{\boldsymbol{h}}_r\in\mathbb{C}^{N_s\times 1}$ represent the MFS $\rightarrow$ target and the target $\rightarrow$ sensors links, respectively, both of which are assumed to be line-of-sight (LoS) links, by properly deploying the MFS to assist sensing [3], [10], [27].[5] According to Fig. 1, $\bar{\boldsymbol{h}}_r$ and $\boldsymbol{h}_r$ are respectively given by

$$\bar{\boldsymbol{h}}_r=e^{-j\frac{2\pi}{\lambda}\left(\bar{\boldsymbol{d}}_x\cos\varphi_h\sin\varphi_v+\bar{\boldsymbol{d}}_z\cos\varphi_v\right)}, \tag{16}$$
$$\boldsymbol{h}_r=e^{-j\frac{2\pi}{\lambda}\left(\boldsymbol{d}_x\cos\varphi_h\sin\varphi_v+\boldsymbol{d}_z\cos\varphi_v\right)}, \tag{17}$$

where $\bar{\boldsymbol{d}}_c\in\mathbb{R}^{N_s\times 1}$ and $\boldsymbol{d}_c\in\mathbb{R}^{N\times 1},\forall c\in\{x,z\}$ denote the Cartesian coordinates of the sensors and A&T&R elements on the c-axis at the MFS, respectively; φ_h and φ_v represent the azimuth and elevation AoA, respectively; and λ denotes the wavelength. Then, at the lth time slot, the echo signal reflected by the MFS at the sensors is given by

$$\boldsymbol{y}_r^l=\tilde{\mathbf{H}}\mathbf{\Phi}_r\mathbf{G}\boldsymbol{x}_l+\tilde{\mathbf{H}}\mathbf{\Phi}_r\boldsymbol{n}_{\mathrm{I}}^l+\boldsymbol{n}_s^l, \tag{18}$$

where $\boldsymbol{n}_s^l\sim\mathcal{CN}\left(\mathbf{0},\sigma_s^2\mathbf{I}_{N_s}\right)$ is the AWGN at the sensors. By stacking $\boldsymbol{y}_r^l$ in (49), we have

$$\underbrace{\left[\boldsymbol{y}_r^1,\ldots,\boldsymbol{y}_r^L\right]}_{\mathbf{Y}_r}=\tilde{\mathbf{H}}\mathbf{\Phi}_r\mathbf{G}\mathbf{X}+\tilde{\mathbf{H}}\mathbf{\Phi}_r\mathbf{N}_{\mathrm{I}}+\underbrace{\left[\boldsymbol{n}_s^1,\ldots,\boldsymbol{n}_s^L\right]}_{\mathbf{N}_s}. \tag{19}$$

2) Derivation of the CRB Matrix: The CRB matrix is an estimation metric used for evaluating the target estimation, which is a lower bound on the variance of the unbiased estimator [3]. In this work, we derive the CRB matrix for the target estimation based on an UPA-type MFS. To proceed, we define the estimation parameters vector as $\boldsymbol{\zeta}=\left[\varphi_h,\varphi_v,\mathrm{Re}\{\alpha\},\mathrm{Im}\{\alpha\}\right]^T$ and the possibility density function (PDF) of $\mathbf{Y}_r$ is $f(\mathbf{Y}_r;\boldsymbol{\zeta})$. Then, the Fisher information matrix

[2]The concept of the nonlinearity of amplifiers at the MFS can be found in [23] and [24], where the kind of nonlinear amplifier includes the solid state power amplifier and the traveling wave tube amplifier, which characterizes the nonlinearity of the amplifier used for boosting incoming signal at the RIS. For simplicity, we consider linear amplifiers employed at the MFS in the proposed scheme, as the linear operation region of the incident signal can be achieved by properly deploying the amplifiers at this area. In addition, the linear operation region considered in this paper can assist in conducting better research for the CRB minimization of ISAC systems with assistance of an MFS to reveal more foresight.

[3]The received signal of users reflected by the target is omitted since its power is extremely weak due to the severe path loss caused by MFE [10]. Moreover, we also ignore signal reflected and transmitted by the MFS more than twice due to the same reason.

[4]As verified in [14], the power of the dynamic noise increases nearly linearly with the amplification factor of the amplifier, and thus demonstrating the correctness of signal expression in (14), for which the dynamic noise power cannot be neglected for the proposed scheme.

[5]The LoS link can be constructed by properly deploying the MFS to better sense the target, and the key parameters for the CSI of MFS $\rightarrow$ target link, i.e., the complex-valued channel coefficient and the angles of target, can be obtained by the multiple signal classification [28]. Additionally, the AoAs of the target changes very slowly between two adjacent coherence blocks, which is sufficient for beamforming design and performing target tracking based on the previous coherence blocks.

$$\gamma_k=\frac{\left|\boldsymbol{h}_k^H\mathbf{\Phi}_t\mathbf{G}\boldsymbol{w}_k\right|^2}{\sum_{j=1,j\neq k}^{K}\left|\boldsymbol{h}_k^H\mathbf{\Phi}_t\mathbf{G}\boldsymbol{w}_j\right|^2+\boldsymbol{h}_k^H\mathbf{\Phi}_t\mathbf{G}\mathbf{R}_s\mathbf{G}^H\mathbf{\Phi}_t^H\boldsymbol{h}_k+\sigma_{\mathrm{I}}^2\left\|\boldsymbol{h}_k^H\mathbf{\Phi}_t\right\|^2+\sigma_u^2}. \tag{15}$$

(FIM) for estimating $\boldsymbol{\zeta}$ is $\mathbf{F}$ [29], with each element given by [30]

$$[\mathbf{F}]_{u,w} = -\mathbb{E}\left\{\frac{\partial^2 \ln f(\mathbf{Y}_r;\boldsymbol{\zeta})}{\partial[\boldsymbol{\zeta}]_u \partial[\boldsymbol{\zeta}]_w}\right\}, \quad \forall u,w=1,\ldots,4. \quad (20)$$

Lemma 1: The FIM, $\mathbf{F}$, is given by

$$\mathbf{F} = \begin{bmatrix} \mathbf{J}_{\boldsymbol{\varphi}\boldsymbol{\varphi}} & \mathbf{J}_{\boldsymbol{\varphi}\boldsymbol{\alpha}} \\ \mathbf{J}_{\boldsymbol{\varphi}\boldsymbol{\alpha}}^H & \mathbf{J}_{\boldsymbol{\alpha}\boldsymbol{\alpha}} \end{bmatrix} \in \mathbb{C}^{4\times 4}, \quad (21)$$

where each block is given by (50)-(52), shown at the bottom of the page 14 in Appendix A.

Proof: Please see Appendix A. ■

Based on **Lemma 1**, the CRB for estimating φ_h and φ_v is derived as

$$\mathrm{CRB}_{\boldsymbol{\varphi}} = \left[\mathbf{F}^{-1}\right]_{1:2,1:2} = \mathbf{E}^{-1}, \quad (22)$$

where

$$\mathbf{F}^{-1} = \begin{bmatrix} \mathbf{E}^{-1} & \bar{\mathbf{F}} \\ \bar{\mathbf{F}}^H & \mathbf{K} \end{bmatrix},$$

with $\mathbf{E} = \mathbf{J}_{\boldsymbol{\varphi}\boldsymbol{\varphi}} - \mathbf{J}_{\boldsymbol{\varphi}\boldsymbol{\alpha}}\mathbf{J}_{\boldsymbol{\alpha}\boldsymbol{\alpha}}^{-1}\mathbf{J}_{\boldsymbol{\varphi}\boldsymbol{\alpha}}^H$ [31].

Remark 2: Due to the introduction of the dynamic noise caused by the amplifier at the MFS, the term of $\mathrm{Tr}\left(\mathbf{C}^{-1}\frac{\partial \mathbf{C}}{\partial \zeta_u}\mathbf{C}^{-1}\frac{\partial \mathbf{C}}{\partial \zeta_w}\right)$ shown in Appendix A used for obtaining elements in the FIM matrix is non-negligible, which is different from previous works that ignore the variance of noise. Therefore, the beamforming vectors and the MFS precoding matrix, $\boldsymbol{w}_k, \forall k$ and $\boldsymbol{\Phi}_r$ should be considered for the term of $\mathrm{Tr}\left(\mathbf{C}^{-1}\frac{\partial \mathbf{C}}{\partial \zeta_u}\mathbf{C}^{-1}\frac{\partial \mathbf{C}}{\partial \zeta_w}\right)$, which impacts the ISAC system assisted by the proposed MFS.

The closed-form CRB matrix is derived based on **Lemma 1**. Given fixed parameters, α, φ_h, and φ_v, and estimated using the maximum likelihood method [10], it becomes necessary to design beamforming strategies that minimize the CRB, thereby enhancing the overall sensing performance. Accordingly, we formulate the CRB minimization problem in the subsections that follow.

E. Problem Formulation

Based on the system model described above, we formulate a CRB minimization problem subject to several practical constraints, including the maximum available power constraints at the BS and the MFS, the SINR constraint, and the coupled or independent phase-shift constraint. The problem is formally stated as follows:

$$\min_{\{\boldsymbol{w}_k\},\mathbf{R}_s,\{\boldsymbol{\Phi}_i\}} \ \mathrm{Tr}\left(\mathrm{CRB}_{\boldsymbol{\varphi}}\right), \quad (23a)$$

$$\text{s.t.} \quad \gamma_k \geq \bar{\gamma}_k, \quad \forall k, \quad (23b)$$

$$\mathbf{R}_s \succeq \mathbf{0}, \quad (23c)$$

$$(1),\ (7)/\ (11),\ (12),\ \text{and}\ (13), \quad (23d)$$

where (23b) denotes the SINR requirement constraint with $\bar{\gamma}_k$ being the minimum communication SINR requirement for the kth user. Problem (23) is challenging to solve due to its non-convex nature and the presence of coupled variables in equations (7)/ (11), (13), (23a), and (23b). These complexities render problem (23) NP-hard. To address this challenge, we propose a set of efficient solution methods, which are detailed in the following sections.

III. Preliminaries and Problem Formulation

To address the non-convex and NP-hard nature of problem (23), we introduce a set of solution methods. First, we decouple the highly coupled variables using the PDD method. Then, based on the PDD framework, we apply the BCD method to decompose problem (23) into multiple subproblems. To proceed, we first transform the original problem into a more tractable form, as detailed in the following subsection.

A. Reformulation of the Original Problem

It is important to note that each block of the CRB matrix in (50)-(52) presents specific challenges that hinder beamforming design: 1) The presence of highly coupled variables as shown

$$\tilde{\mathbf{J}}_{\boldsymbol{\varphi}\boldsymbol{\varphi}} = \underbrace{2|\alpha|^2 L\mathrm{Re}\left\{\begin{bmatrix} \mathrm{Tr}\left(\tilde{\mathbf{B}}^{-1}\dot{\mathbf{H}}_{\varphi_h}\boldsymbol{\Omega}\dot{\mathbf{H}}_{\varphi_h}^H\right) & \mathrm{Tr}\left(\tilde{\mathbf{B}}^{-1}\dot{\mathbf{H}}_{\varphi_v}\boldsymbol{\Omega}\dot{\mathbf{H}}_{\varphi_h}^H\right) \\ \mathrm{Tr}\left(\tilde{\mathbf{B}}^{-1}\dot{\mathbf{H}}_{\varphi_h}\boldsymbol{\Omega}\dot{\mathbf{H}}_{\varphi_v}^H\right) & \mathrm{Tr}\left(\tilde{\mathbf{B}}^{-1}\dot{\mathbf{H}}_{\varphi_v}\boldsymbol{\Omega}\dot{\mathbf{H}}_{\varphi_v}^H\right) \end{bmatrix}\right\}}_{\bar{\mathbf{J}}_{\boldsymbol{\varphi}\boldsymbol{\varphi}}} + Y_1 \underbrace{\begin{bmatrix} \mathrm{Tr}\left(\tilde{\mathbf{B}}^{-1}\dot{\bar{\mathbf{H}}}_{\varphi_h}\tilde{\mathbf{B}}^{-1}\dot{\bar{\mathbf{H}}}_{\varphi_h}\right) & \mathrm{Tr}\left(\tilde{\mathbf{B}}^{-1}\dot{\bar{\mathbf{H}}}_{\varphi_h}\tilde{\mathbf{B}}^{-1}\dot{\bar{\mathbf{H}}}_{\varphi_v}\right) \\ \mathrm{Tr}\left(\tilde{\mathbf{B}}^{-1}\dot{\bar{\mathbf{H}}}_{\varphi_v}\tilde{\mathbf{B}}^{-1}\dot{\bar{\mathbf{H}}}_{\varphi_h}\right) & \mathrm{Tr}\left(\tilde{\mathbf{B}}^{-1}\dot{\bar{\mathbf{H}}}_{\varphi_v}\tilde{\mathbf{B}}^{-1}\dot{\bar{\mathbf{H}}}_{\varphi_v}\right) \end{bmatrix}}_{\bar{\bar{\mathbf{J}}}_{\boldsymbol{\varphi}\boldsymbol{\varphi}}}, \quad (24)$$

$$\tilde{\mathbf{J}}_{\boldsymbol{\varphi}\boldsymbol{\alpha}} = \underbrace{2\alpha^* L\mathrm{Re}\left\{\begin{bmatrix} \mathrm{Tr}\left(\tilde{\mathbf{B}}^{-1}\mathbf{H}\boldsymbol{\Omega}\dot{\mathbf{H}}_{\varphi_h}^H\right) & j\mathrm{Tr}\left(\tilde{\mathbf{B}}^{-1}\mathbf{H}\boldsymbol{\Omega}\dot{\mathbf{H}}_{\varphi_h}^H\right) \\ \mathrm{Tr}\left(\tilde{\mathbf{B}}^{-1}\mathbf{H}\boldsymbol{\Omega}\dot{\mathbf{H}}_{\varphi_v}^H\right) & j\mathrm{Tr}\left(\tilde{\mathbf{B}}^{-1}\mathbf{H}\boldsymbol{\Omega}\dot{\mathbf{H}}_{\varphi_v}^H\right) \end{bmatrix}\right\}}_{\bar{\mathbf{J}}_{\boldsymbol{\varphi}\boldsymbol{\alpha}}} + Y_2 \underbrace{\begin{bmatrix} \alpha_{\mathrm{R}}\mathrm{Tr}\left(\tilde{\mathbf{B}}^{-1}\dot{\bar{\mathbf{H}}}_{\varphi_h}\tilde{\mathbf{B}}^{-1}\bar{\mathbf{H}}\right) & \alpha_{\mathrm{S}}\mathrm{Tr}\left(\tilde{\mathbf{B}}^{-1}\dot{\bar{\mathbf{H}}}_{\varphi_h}\tilde{\mathbf{B}}^{-1}\bar{\mathbf{H}}\right) \\ \alpha_{\mathrm{R}}\mathrm{Tr}\left(\tilde{\mathbf{B}}^{-1}\dot{\bar{\mathbf{H}}}_{\varphi_v}\tilde{\mathbf{B}}^{-1}\bar{\mathbf{H}}\right) & \alpha_{\mathrm{S}}\mathrm{Tr}\left(\tilde{\mathbf{B}}^{-1}\dot{\bar{\mathbf{H}}}_{\varphi_v}\tilde{\mathbf{B}}^{-1}\bar{\mathbf{H}}\right) \end{bmatrix}}_{\bar{\bar{\mathbf{J}}}_{\boldsymbol{\varphi}\boldsymbol{\alpha}}}, \quad (25)$$

$$\tilde{\mathbf{J}}_{\boldsymbol{\alpha}\boldsymbol{\alpha}} = 2L\mathrm{Tr}\left(\tilde{\mathbf{B}}^{-1}\mathbf{H}\boldsymbol{\Omega}\mathbf{H}^H\right)\mathbf{I}_2 + \underbrace{4L\sigma_{\mathrm{I}}^4 Z\left\|\boldsymbol{\Phi}_r\right\|_{\mathrm{F}}^2}_{Y_3} \underbrace{\begin{bmatrix} \alpha_{\mathrm{R}}^2\mathrm{Tr}\left(\tilde{\mathbf{B}}^{-1}\bar{\mathbf{H}}\tilde{\mathbf{B}}^{-1}\bar{\mathbf{H}}\right) & \alpha_{\mathrm{R}}\alpha_{\mathrm{S}}\mathrm{Tr}\left(\tilde{\mathbf{B}}^{-1}\bar{\mathbf{H}}\tilde{\mathbf{B}}^{-1}\bar{\mathbf{H}}\right) \\ \alpha_{\mathrm{R}}\alpha_{\mathrm{S}}\mathrm{Tr}\left(\tilde{\mathbf{B}}^{-1}\bar{\mathbf{H}}\tilde{\mathbf{B}}^{-1}\bar{\mathbf{H}}\right) & \alpha_{\mathrm{S}}^2\mathrm{Tr}\left(\tilde{\mathbf{B}}^{-1}\bar{\mathbf{H}}\tilde{\mathbf{B}}^{-1}\bar{\mathbf{H}}\right) \end{bmatrix}}_{\bar{\bar{\mathbf{J}}}_{\boldsymbol{\alpha}\boldsymbol{\alpha}}}. \quad (26)$$

in the first matrix in (50)-(52), i.e., $\mathbf{\Phi}_r\mathbf{G}\mathbf{R}_x\mathbf{G}^H\mathbf{\Phi}_r^H$; 2) The occurrence of a fourth-order term, specifically the Frobenius norm raised to the fourth power, i.e., $\|\mathbf{\Phi}_r\|_{\mathrm{F}}^4$; 3) The presence of a matrix inverse involving optimization variables, i.e., $\tilde{\mathbf{B}}^{-1} = (|\alpha|^2\sigma_{\mathrm{I}}^2\|\mathbf{\Phi}_r\|_{\mathrm{F}}^2\bar{\mathbf{H}} + \sigma_s^2\mathbf{I}_{N_s})^{-1}$; 4) For the coupled phase-shift case, the constraint in (7) involves the norm of a phase difference, which is nontrivial to handle. To address these challenges, we first adopt the PDD method. Specifically, we substitute $\mathbf{\Phi}_r\mathbf{G}\mathbf{R}_x\mathbf{G}^H\mathbf{\Phi}_r^H$, $\|\mathbf{\Phi}_r\|_{\mathrm{F}}^2$, and $\boldsymbol{\phi}_i$ with $\mathbf{\Omega}$, Z, and $\tilde{\boldsymbol{\phi}}_i = [\sqrt{p_1}\tilde{\varrho}_{i,1}e^{j\tilde{\theta}_{i,1}}, \ldots, \sqrt{p_N}\tilde{\varrho}_{i,N}e^{j\tilde{\theta}_{i,N}}]^T$, such that $\mathbf{\Omega} = \mathbf{\Phi}_r\mathbf{G}\mathbf{R}_x\mathbf{G}^H\mathbf{\Phi}_r^H$, $Z = \|\mathbf{\Phi}_r\|_{\mathrm{F}}^2$, and $\tilde{\boldsymbol{\phi}}_i = \boldsymbol{\phi}_i, \forall i$. This reformulation moves the highly coupled terms into the objective function, leading to a more tractable structure for the associated constraints. Then, we have the following proposition.

Proposition 1: By introducing an auxiliary variable $\mathbf{A} \in \mathbb{H}^2$, problem (23) in coupled phase-shift case can be equivalently transformed into

$$\min_{\mathbf{\Delta}} \quad \mathrm{Obj}, \tag{27a}$$

$$\text{s.t.} \quad \begin{bmatrix} \tilde{\mathbf{J}}_{\boldsymbol{\varphi}\boldsymbol{\varphi}} - \mathbf{A} & \tilde{\mathbf{J}}_{\boldsymbol{\varphi}\boldsymbol{\alpha}} \\ \tilde{\mathbf{J}}_{\boldsymbol{\varphi}\boldsymbol{\alpha}}^H & \tilde{\mathbf{J}}_{\boldsymbol{\alpha}\boldsymbol{\alpha}} \end{bmatrix} \succeq \mathbf{0}, \tag{27b}$$

$$P_{\mathrm{R}} \le P_{\mathrm{R}}^{\max}, \tag{27c}$$

$$\mathbf{R}_x \succeq \sum_{k=1}^{K} \boldsymbol{w}_k\boldsymbol{w}_k^H, \ \mathbf{A} \succeq \mathbf{0}, \tag{27d}$$

$$\tilde{\beta}_{r,n}^2 + \tilde{\beta}_{t,n}^2 \le P_{\mathrm{A}}^{\max}, \quad \left|\tilde{\theta}_{t,n} - \tilde{\theta}_{r,n}\right| = \frac{\pi}{2} \text{ or } \frac{3\pi}{2}, \quad \tilde{\beta}_{i,n} \ge 0, \quad \tilde{\theta}_{i,n} \in [0, 2\pi), \quad \forall i, n, \tag{27e}$$

$$(1), \ (23b), \tag{27f}$$

where $P_{\mathrm{R}} = \mathrm{Tr}\left(\mathbf{\Phi}_t\mathbf{G}\mathbf{R}_x\mathbf{G}^H\mathbf{\Phi}_t^H + \mathbf{\Omega}\right) + \sum_i \sigma_{\mathrm{I}}^2\|\mathbf{\Phi}_i\|_{\mathrm{F}}^2$, $\mathrm{Obj} = \mathrm{Tr}(\mathbf{A}^{-1}) + \frac{1}{2\mu}\Big(\|\mathbf{\Omega} - \mathbf{\Phi}_r\mathbf{G}\mathbf{R}_x\mathbf{G}^H\mathbf{\Phi}_r^H + \mu\mathbf{\Psi}\|_{\mathrm{F}}^2 + |Z - \|\mathbf{\Phi}_r\|_{\mathrm{F}}^2 + \mu\psi_z|^2 + \sum_i \|\tilde{\boldsymbol{\phi}}_i - \boldsymbol{\phi}_i + \mu\boldsymbol{\psi}_i\|^2\Big)$, $\mathbf{\Delta} \triangleq \{\mathbf{R}_x, \{\boldsymbol{w}_k\}, \{\mathbf{\Phi}_i\}, \mathbf{\Omega}, \{\tilde{\boldsymbol{\phi}}_i\}, \mathbf{A}, Z, \tilde{\mathbf{B}}\}$; $\mu > 0$ denotes the penalty factor; $\mathbf{\Psi}$, ψ_z, and $\boldsymbol{\psi}_i$ are Lagrangian dual variables; and $\tilde{\mathbf{J}}_{\boldsymbol{\varphi}\boldsymbol{\varphi}}$, $\tilde{\mathbf{J}}_{\boldsymbol{\varphi}\boldsymbol{\alpha}}$, and $\tilde{\mathbf{J}}_{\boldsymbol{\alpha}\boldsymbol{\alpha}}$ are given in (24), (25), and (26), shown at the bottom of the previous page, respectively. Here, $Y_1 = L|\alpha|^4\sigma_{\mathrm{I}}^4 Z\|\mathbf{\Phi}_r\|_{\mathrm{F}}^2$ and $Y_2 = 2L|\alpha|^2\sigma_{\mathrm{I}}^4 Z\|\mathbf{\Phi}_r\|_{\mathrm{F}}^2$.

Proof: First, the terms $\|\mathbf{\Omega} - \mathbf{\Phi}_r\mathbf{G}\mathbf{R}_x\mathbf{G}^H\mathbf{\Phi}_r^H + \mu\mathbf{\Psi}\|_{\mathrm{F}}^2$, $|Z - \|\mathbf{\Phi}_r\|_{\mathrm{F}}^2 + \mu\psi_z|^2$, and $\sum_i \left\|\tilde{\boldsymbol{\phi}}_i - \boldsymbol{\phi}_i + \mu\boldsymbol{\psi}_i\right\|^2$ in (27a) means that $\mathbf{\Omega} = \mathbf{\Phi}_r\mathbf{G}\mathbf{R}_x\mathbf{G}^H\mathbf{\Phi}_r^H$, $Z = \|\mathbf{\Phi}_r\|_{\mathrm{F}}^2$, and $\tilde{\boldsymbol{\phi}}_i = \boldsymbol{\phi}_i, \forall i$ according to the PDD structure [32], with μ being the penalty factor as well as $\mathbf{\Psi}$ and $\boldsymbol{\psi}_i$ being the Lagrangian dual variables. In addition, we can derive (27e) easily by combining (7) and (12). Moreover, according to Lemma 1 and Proposition 1 as in [10], and $\mathbf{R}_x = \sum_{k=1}^{K}\boldsymbol{w}_k\boldsymbol{w}_k^H + \mathbf{R}_s$, problem (23) can be equivalently transformed into (27), which is a Lagrangian augmented problem of the original problem (23). ■

Similar to **Proposition 1**, the original problem (23) with independent phase-shift can be equivalently transformed into

$$\min_{\bar{\mathbf{\Delta}}} \quad \mathrm{Tr}\left(\mathbf{A}^{-1}\right) + \frac{1}{2\mu}\left(\left\|\mathbf{\Omega} - \mathbf{\Phi}_r\mathbf{G}\mathbf{R}_x\mathbf{G}^H\mathbf{\Phi}_r^H + \mu\mathbf{\Psi}\right\|_{\mathrm{F}}^2 + \left|Z - \|\mathbf{\Phi}_r\|_{\mathrm{F}}^2 + \mu\psi_z\right|^2\right), \tag{28a}$$

Algorithm 1 PDD Algorithm for Solving Problem (27) or (28)

Initialization: Iteration index $u = 1$, $\{\mathbf{\Phi}_i\}$, $\{\tilde{\boldsymbol{\phi}}_i\}$, $\tilde{\mathbf{B}}$, $\mathbf{\Psi}^{(1)}$, $\psi_z^{(1)}$, and $\{\boldsymbol{\psi}_i^{(1)}\}$.
repeat
  Optimize augmented Lagrangian problem (27).
  Output $\{\mathbf{\Phi}_i\}$, $\mathbf{\Omega}$, $\mathbf{R}_x$, Z, and $\{\tilde{\boldsymbol{\phi}}_i\}$.
  Calculate constraint violation $\epsilon = \max(\|\mathbf{\Omega} - \mathbf{\Phi}_r\mathbf{G}\mathbf{R}_x\mathbf{G}^H\mathbf{\Phi}_r^H\|_\infty, |Z - \|\mathbf{\Phi}_r\|_{\mathrm{F}}^2|, \|\tilde{\boldsymbol{\phi}}_t - \boldsymbol{\phi}_t\|_\infty, \|\tilde{\boldsymbol{\phi}}_r - \boldsymbol{\phi}_r\|_\infty)$ for problem (27) or $\epsilon = \max(\|\mathbf{\Omega} - \mathbf{\Phi}_r\mathbf{G}\mathbf{R}_x\mathbf{G}^H\mathbf{\Phi}_r^H\|_\infty, |Z - \|\mathbf{\Phi}_r\|_{\mathrm{F}}^2|)$ for problem (28).
  if $\epsilon \le \bar{\epsilon}$ **then**
    Update $\mathbf{\Psi}^{(u+1)} = \mathbf{\Psi}^{(u)} + \frac{1}{\mu}(\mathbf{\Omega} - \mathbf{\Phi}_r\mathbf{G}\mathbf{R}_x\mathbf{G}^H\mathbf{\Phi}_r^H)$.
    Update $\psi_z^{(u+1)} = \psi_z^{(u)} + \frac{1}{\mu}(Z - \|\mathbf{\Phi}_r\|_{\mathrm{F}}^2)$.
    Update $\boldsymbol{\psi}_i^{(u+1)} = \boldsymbol{\psi}_i^{(u)} + \frac{1}{\mu}(\tilde{\boldsymbol{\phi}}_i - \boldsymbol{\phi}_i)$ for problem (27).
  else
    Update $\mu^{(u+1)} = c\mu^{(u)}$.
  end if
  Update $\bar{\epsilon} = c\epsilon$.
  Set $u = u + 1$.
until $\epsilon \le \tilde{\epsilon}$.

$$\text{s.t.} \quad \left|[\mathbf{\Phi}_t]_{n,n}\right|^2 + \left|[\mathbf{\Phi}_r]_{n,n}\right|^2 \le P_{\mathrm{A}}^{\max}, \quad \forall n, \tag{28b}$$

$$(1), \ (23b), \ (27b), \ (27c), \ (27d), \tag{28c}$$

where $\bar{\mathbf{\Delta}} \triangleq \{\mathbf{R}_x, \{\boldsymbol{w}_k\}, \{\mathbf{\Phi}_i\}, \mathbf{\Omega}, \mathbf{A}, Z, \tilde{\mathbf{B}}\}$. The details of the PDD method for solving problem (27) or (28) are given in **Algorithm 1**, where $\bar{\epsilon}$ and $\tilde{\epsilon}$ denote the initializing constraint violation threshold and constraint violation threshold required for convergence, respectively, and c denotes the reduction factor.

B. Challenges and Solution Strategies for the Formulated Problems

Although the original problem (23) is transformed into a more tractable form in (27) based on the PDD method, the non-convexity remains. In particular, we can observe that the terms, $\mathbf{\Phi}_r\mathbf{G}\mathbf{R}_x\mathbf{G}\mathbf{\Phi}_r^H$ and $\|\mathbf{\Phi}_r\|_{\mathrm{F}}^2$, lead to non-convexity of the objective function, and the non-convexity of constraints in (23b), (27b), (27c), and (27e) is due to the same reason. Therefore, we employ the BCD method to decompose problem (27) into three (or two) subproblems, thereby decoupling the optimization variables and simplifying the solution process. Specifically, for the coupled phase-shift case, there are three subproblems, i.e., subproblem 1 (optimizing $\mathbf{R}_x$ and $\boldsymbol{w}_k$), subproblem 2 (optimizing $\{\mathbf{\Phi}_i\}$), and subproblem 3 (optimizing $\{\tilde{\boldsymbol{\phi}}_i\}$); while for the independent phase-shift case, there are two subproblems, i.e., subproblem 1 and subproblem 2, mentioned above. The methods for solving these subproblems are desribed in the following sections. Moreover, since the inverse of the matrix $\tilde{\mathbf{B}}$, $\tilde{\mathbf{B}}^{-1}$, contains the optimization variable $\mathbf{\Phi}_r$, it introduces additional complexity in handling the CRB matrix, particularly in conjunction with equations (24)-(26). To address this challenge, we approximately update $\tilde{\mathbf{B}}$ in each BCD iteration, after solving the three (or two) subproblems corresponding to the coupled or independent phase-shift cases, respectively, and continue this process until convergence is achieved [17].

IV. CRB Optimization for Coupled Phase-Shift Case Based on BCD Method

For the coupled phase-shift case, problem (27) is decomposed into three subproblems. The solution methods for these subproblems are presented in the following subsections.

A. Optimize Beamformer at the BS

For any given $\{\mathbf{\Phi}_i\}$, $\{\tilde{\boldsymbol{\phi}}_i\}$, and $\tilde{\mathbf{B}}$, we have the following subproblem with respect to optimizing $\mathbf{R}_x$ and $\{\boldsymbol{w}_k\}$

$$\min_{\mathbf{\Delta}_w} \quad \mathrm{Tr}\left(\mathbf{A}^{-1}\right)+\frac{1}{2\mu}\left(\left\|\mathbf{\Omega}-\mathbf{\Phi}_r\mathbf{G}\mathbf{R}_x\mathbf{G}^H\mathbf{\Phi}_r^H+\mu\mathbf{\Psi}\right\|_{\mathrm{F}}^2 + \left|Z-\|\mathbf{\Phi}_r\|_{\mathrm{F}}^2+\mu\psi_z\right|^2\right), \tag{29a}$$

$$\text{s.t.} \quad (1),\ (23b),\ (27b),\ (27c),\ (27d), \tag{29b}$$

where $\mathbf{\Delta}_w \triangleq \{\mathbf{R}_x,\{\boldsymbol{w}_k\},\mathbf{\Omega},\mathbf{A},Z\}$. It can be seen that constraint (23b) is non-convex due to the fractional form and quadratic term arising from $\boldsymbol{w}_k$. To address this, we first reformulate constraint (23b) into the following by letting $\bar{\mathbf{R}}_k=\boldsymbol{w}_k\boldsymbol{w}_k^H$:

$$\left(1+\frac{1}{\bar{\gamma}_k}\right)\mathrm{Tr}\left(\tilde{\mathbf{H}}_k\bar{\mathbf{R}}_k\right)\geq \mathrm{Tr}\left(\tilde{\mathbf{H}}_k\mathbf{R}_x\right)+\delta_k, \quad \forall k, \tag{30}$$

where $\tilde{\mathbf{H}}_k=\tilde{\boldsymbol{h}}_k\tilde{\boldsymbol{h}}_k^H$ with $\tilde{\boldsymbol{h}}_k=\mathbf{G}^H\mathbf{\Phi}_t^H\boldsymbol{h}_k$, and $\delta_k=\sigma_{\mathrm{I}}^2\|\boldsymbol{h}_k^H\mathbf{\Phi}_t\|^2+\sigma_u^2$. Due to the introduction of $\bar{\mathbf{R}}_k=\boldsymbol{w}_k\boldsymbol{w}_k^H$, the rank-one constraint is unavoidable, leading to the following reformulated problem:

$$\min_{\bar{\mathbf{\Delta}}_w} \quad \mathrm{Tr}\left(\mathbf{A}^{-1}\right)+\frac{1}{2\mu}\left(\left\|\mathbf{\Omega}-\mathbf{\Phi}_r\mathbf{G}\mathbf{R}_x\mathbf{G}^H\mathbf{\Phi}_r^H+\mu\mathbf{\Psi}\right\|_{\mathrm{F}}^2 + \left|Z-\|\mathbf{\Phi}_r\|_{\mathrm{F}}^2+\mu\psi_z\right|^2\right), \tag{31a}$$

$$\text{s.t.} \quad \mathrm{Rank}\left(\bar{\mathbf{R}}_k\right)=1, \quad \forall k, \tag{31b}$$

$$\bar{\mathbf{R}}_k \succeq \mathbf{0}, \tag{31c}$$

$$(1),\ (27b),\ (27c),\ (27d),\ (30) \tag{31d}$$

where $\bar{\mathbf{\Delta}}_w \triangleq \{\mathbf{R}_x,\{\bar{\mathbf{R}}_k\},\mathbf{\Omega},\mathbf{A},Z\}$. Constraints (31b) and (31c) are necessary due to the introduction of $\bar{\mathbf{R}}_k=\boldsymbol{w}_k\boldsymbol{w}_k^H$. Although constraint (31b) is non-convex, it can be relaxed or removed to improve tractability. Subsequently, problem (31) can be solved using convex optimization solvers such as CVX [33]. However, then resulting solution for $\bar{\mathbf{R}}_k$ may not satisfy the rank-one requirement, since constraint (31b) is omitted in the relaxed formulation. Fortunately, a rank-one solution can be constructed from the obtained $\bar{\mathbf{R}}_k$. Specifically, by denoting the solution of the relaxed version of problem (31) as $\left\{\mathbf{R}_x^\star,\bar{\mathbf{R}}_1^\star,\ldots,\bar{\mathbf{R}}_K^\star\right\}$, the globally optimal solution of problem (31), $\left\{\hat{\mathbf{R}}_x,\hat{\bar{\mathbf{R}}}_1,\ldots,\hat{\bar{\mathbf{R}}}_K\right\}$, is given in the following according to [20, Theorem 1]

$$\hat{\mathbf{R}}_x=\mathbf{R}_x^\star, \quad \hat{\bar{\mathbf{R}}}_k=\boldsymbol{w}_k^\star\left(\boldsymbol{w}_k^\star\right)^H, \quad \forall k, \tag{32}$$

where $\boldsymbol{w}_k^\star=\left(\tilde{\boldsymbol{h}}_k^H\bar{\mathbf{R}}_k^\star\tilde{\boldsymbol{h}}_k\right)^{-\frac{1}{2}}\bar{\mathbf{R}}_k^\star\tilde{\boldsymbol{h}}_k$.

B. Optimize Beamforming Matrix at the MFS

For any given $\{\tilde{\boldsymbol{\phi}}_i\}$, $\mathbf{R}_x$, $\{\boldsymbol{w}_k\}$, $\mathbf{\Omega}$, $\mathbf{A}$, Z, and $\tilde{\mathbf{B}}$, the problem of optimizing $\{\mathbf{\Phi}_i\}$ is expressed as follows:

$$\min_{\{\mathbf{\Phi}_i\}} \left\|\mathbf{\Omega}-\mathbf{\Phi}_r\mathbf{G}\mathbf{R}_x\mathbf{G}^H\mathbf{\Phi}_r^H+\mu\mathbf{\Psi}\right\|_{\mathrm{F}}^2+\left|Z-\|\mathbf{\Phi}_r\|_{\mathrm{F}}^2+\mu\psi_z\right|^2 + \sum_i\left\|\tilde{\boldsymbol{\phi}}_i-\boldsymbol{\phi}_i+\mu\boldsymbol{\psi}_i\right\|^2, \tag{33a}$$

$$\text{s.t.} \quad (23b),\ (27b),\ (27c). \tag{33b}$$

Note that the objective function and constraints in (33) are non-convex, due to the presence of coupled variables $\mathbf{\Phi}_i$. To address this challenge, we first let $\bar{\mathbf{V}}_i=\bar{\boldsymbol{\phi}}_i\bar{\boldsymbol{\phi}}_i^H$ with $\bar{\boldsymbol{\phi}}_i=[\boldsymbol{\phi}_i^T,1]^T$. Then, the eigenvalue decomposition of $\mathbf{G}\mathbf{R}_x\mathbf{G}^H$ is $\mathbf{G}\mathbf{R}_x\mathbf{G}^H=\sum_{b=1}^B\mathrm{diag}(\mathbf{Q}_b)(\mathrm{diag}(\mathbf{Q}_b))^H$, where $\mathbf{Q}_b=\lambda_b\mathrm{Diag}(\boldsymbol{u}_b)$ with λ_b and $\boldsymbol{u}_b$ denoting the bth eigenvalue and the corresponding eigenvector, respectively. Based on this, problem (33) can be reformulated as

$$\min_{\{\bar{\mathbf{V}}_i\}} \left\|\mathbf{\Omega}-\sum_{b=1}^B\bar{\mathbf{Q}}_b\bar{\mathbf{V}}_r\bar{\mathbf{Q}}_b^H+\mu\mathbf{\Psi}\right\|_{\mathrm{F}}^2+\left|Z-\mathrm{Tr}\left(\tilde{\mathbf{V}}_r\right)+\mu\psi_z\right|^2 + \sum_i\mathrm{Tr}\left(\mathbf{\Xi}_i\bar{\mathbf{V}}_i\right), \tag{34a}$$

$$\text{s.t.} \quad \tilde{\gamma}_k\mathrm{Tr}\left(\bar{\bar{\mathbf{H}}}_k\bar{\mathbf{V}}_t\right)\geq\mathrm{Tr}\left(\bar{\mathbf{U}}_k\bar{\mathbf{V}}_t^*\right)+\sigma_{\mathrm{I}}^2\mathrm{Tr}\left(\hat{\bar{\mathbf{H}}}_k\bar{\mathbf{V}}_t^*\right), \quad \forall k, \tag{34b}$$

$$\begin{bmatrix}\tilde{\tilde{\mathbf{J}}}_{\varphi\varphi}-\mathbf{A} & \tilde{\tilde{\mathbf{J}}}_{\varphi\alpha}\\ \tilde{\tilde{\mathbf{J}}}_{\varphi\alpha}^H & \tilde{\tilde{\mathbf{J}}}_{\alpha\alpha}\end{bmatrix}\succeq\mathbf{0}, \tag{34c}$$

$$\sum_{b=1}^B\mathrm{Tr}\left(\bar{\mathbf{Q}}_b\bar{\mathbf{V}}_t\bar{\mathbf{Q}}_b^H\right)+\mathrm{Tr}\left(\mathbf{\Omega}\right)+\tilde{M}\leq P_{\mathrm{R}}^{\max}, \tag{34d}$$

$$\bar{\mathbf{V}}_i\succeq\mathbf{0}, \quad \forall i, \tag{34e}$$

$$\mathrm{Rank}\left(\bar{\mathbf{V}}_i\right)=1, \quad \forall i, \tag{34f}$$

$$\left[\bar{\mathbf{V}}_i\right]_{N+1,N+1}=1, \quad \forall i, \tag{34g}$$

where

$$\mathbf{\Xi}_i=\begin{bmatrix}\mathbf{I}_N & \tilde{\boldsymbol{\phi}}_i\\ \tilde{\boldsymbol{\phi}}_i^H & 0\end{bmatrix}, \quad \hat{\bar{\mathbf{H}}}_k=\begin{bmatrix}\mathrm{Diag}\left(\boldsymbol{h}_k^H\right)\mathrm{Diag}\left(\boldsymbol{h}_k\right) & \mathbf{0}_{N\times1}\\ \mathbf{0}_{1\times N} & 0\end{bmatrix},$$

$$\bar{\bar{\mathbf{H}}}_k=\begin{bmatrix}\bar{\boldsymbol{h}}_k\bar{\boldsymbol{h}}_k^H & \mathbf{0}_{N\times1}\\ \mathbf{0}_{1\times N} & 0\end{bmatrix}, \quad \bar{\mathbf{U}}_k=\begin{bmatrix}\mathbf{U}_k & \mathbf{0}_{N\times1}\\ \mathbf{0}_{1\times N} & 0\end{bmatrix},$$

with $\bar{\boldsymbol{h}}_k=\mathrm{Diag}(\boldsymbol{w}_k^H\mathbf{G}^H)\boldsymbol{h}_k$ and $\mathbf{U}_k=\mathrm{Diag}\left(\boldsymbol{h}_k^H\right)\mathbf{G}\mathbf{R}_x\mathbf{G}^H\mathrm{Diag}\left(\boldsymbol{h}_k\right)$; $\tilde{\gamma}_k=1+\frac{1}{\bar{\gamma}_k}$; $\tilde{M}=\sigma_{\mathrm{I}}^2\mathrm{Tr}\left(\bar{\mathbf{V}}_t+\bar{\mathbf{V}}_r\right)$; $\tilde{\mathbf{V}}_r=[\bar{\mathbf{V}}_r]_{1:N,1:N}$; $\tilde{\tilde{\mathbf{J}}}_{\varphi\varphi}=\bar{\mathbf{J}}_{\varphi\varphi}+\tilde{Y}_1\bar{\bar{\mathbf{J}}}_{\varphi\varphi}$, $\tilde{\tilde{\mathbf{J}}}_{\varphi\alpha}=\bar{\mathbf{J}}_{\varphi\alpha}+\tilde{Y}_2\bar{\bar{\mathbf{J}}}_{\varphi\alpha}$, and $\tilde{\tilde{\mathbf{J}}}_{\alpha\alpha}=\bar{\mathbf{J}}_{\alpha\alpha}+\tilde{Y}_3\bar{\bar{\mathbf{J}}}_{\alpha\alpha}$ with $\tilde{Y}_1=L|\alpha|^4\sigma_{\mathrm{I}}^4Z\mathrm{Tr}(\tilde{\mathbf{V}}_r)$, $\tilde{Y}_2=2L|\alpha|^2\sigma_{\mathrm{I}}^4Z\mathrm{Tr}(\tilde{\mathbf{V}}_r)$, and $\tilde{Y}_3=4L\sigma_{\mathrm{I}}^4Z\mathrm{Tr}(\tilde{\mathbf{V}}_r)$, respectively; and $\bar{\mathbf{Q}}_b=[\mathbf{Q}_b,\mathbf{0}_{N\times1}]$. It can be seen that, after dropping the non-convex rank-one constraint in (34f), problem (34) is convex with respect to $\bar{\mathbf{V}}_i$, and thus it can be readily solved using existing solvers [33]. The rank-one solution can be recovered using Gaussian randomization or eigenvalue decomposition. Fortunately, for the relaxed version of problem (34), our numerical evaluations indicate that a rank-one solution can always be obtained in the coupled phase-shift case. As a result, the rank-one solution can be efficiently recovered via eigenvalue decomposition without any performance loss.

C. Optimize Auxiliary Variables

For any given $\mathbf{R}_x$, $\{\boldsymbol{w}_k\}$, $\{\boldsymbol{\Phi}_i\}$, $\boldsymbol{\Omega}$, $\mathbf{A}$, Z, and $\tilde{\mathbf{B}}$, the problem with respect to $\{\tilde{\boldsymbol{\phi}}_i\}$ is given by

$$\min_{\{\tilde{\boldsymbol{\phi}}_i\}} \quad \sum_i \left\| \tilde{\boldsymbol{\phi}}_i - \boldsymbol{\phi}_i + \mu \boldsymbol{\psi}_i \right\|^2, \tag{35a}$$

$$\text{s.t.} \quad (27e). \tag{35b}$$

Note that problem (35) is non-convex due to the quadratic terms and phase difference constraint as in (27e). To address this challenge, we first transform problem (35) into the following

$$\min_{\{\tilde{\beta}_{i,n}\},\{\tilde{\theta}_{i,n}\}} \sum_i \sum_{n=1}^{N} \left(\tilde{\beta}_{i,n}^2 + 2\mathrm{Re}\left\{ \chi_{i,n}^* \tilde{\beta}_{i,n} e^{j\tilde{\theta}_{i,n}} \right\} \right), \tag{36a}$$

$$\text{s.t.} \quad (27e), \tag{36b}$$

where $\chi_{i,n} = [-\boldsymbol{\phi}_i + \mu \boldsymbol{\psi}_i]_n$. It can be observed that the optimization variables $\tilde{\beta}_{i,n}$ and $\tilde{\theta}_{i,n}$ are coupled. To address this, we employ the alternating optimization (AO) method, which splits problem (36) into two subproblems for improved tractability. The first subproblem optimizes $\{\tilde{\beta}_{i,n}\}$, and the second subproblem optimizes $\{\tilde{\theta}_{i,n}\}$.

1) Optimize $\{\tilde{\beta}_{i,n}\}$: For any given $\{\tilde{\theta}_{i,n}\}$, the subproblem of optimizing $\{\tilde{\beta}_{i,n}\}$ is formulated as follows:

$$\min_{\{\tilde{\beta}_{i,n}\}} \quad \sum_i \sum_{n=1}^{N} \left(\tilde{\beta}_{i,n}^2 + 2\mathrm{Re}\left\{ \chi_{i,n}^* \tilde{\beta}_{i,n} e^{j\tilde{\theta}_{i,n}} \right\} \right), \tag{37a}$$

$$\text{s.t.} \quad \tilde{\beta}_{t,n}^2 + \tilde{\beta}_{r,n}^2 \le P_{\mathrm{A}}^{\max}, \quad \tilde{\beta}_{i,n} \ge 0, \quad \forall i,n. \tag{37b}$$

To solve problem (37), we have the following proposition.

Proposition 2: By letting $a_{i,n} = 2\mathrm{Re}\{\chi_{i,n}^* e^{j\tilde{\theta}_{i,n}}\}, \forall i,n$, the optimal closed-form solution of problem (37) is given by

1) When $a_{t,n} \ge 0$ and $a_{r,n} \ge 0$:

$$\tilde{\beta}_{r,n} = 0, \quad \tilde{\beta}_{t,n} = 0. \tag{38}$$

2) When $a_{t,n} < 0$ and $a_{r,n} \ge 0$:

$$\begin{cases} \tilde{\beta}_{r,n} = 0 \text{ and } \tilde{\beta}_{t,n} = -\dfrac{a_{t,n}}{2}, & \text{if } 1 \ge \left|\frac{a_{t,n}}{2\sqrt{P_{\mathrm{A}}^{\max}}}\right|, \\ \tilde{\beta}_{r,n} = 0 \text{ and } \tilde{\beta}_{t,n} = \sqrt{P_{\mathrm{A}}^{\max}}, & \text{Otherwise.} \end{cases} \tag{39}$$

3) When $a_{t,n} \ge 0$ and $a_{r,n} < 0$:

$$\begin{cases} \tilde{\beta}_{r,n} = -\dfrac{a_{r,n}}{2} \text{ and } \tilde{\beta}_{t,n} = 0, & \text{if } 1 \ge \left|\frac{a_{r,n}}{2\sqrt{P_{\mathrm{A}}^{\max}}}\right|, \\ \tilde{\beta}_{r,n} = \sqrt{P_{\mathrm{A}}^{\max}} \text{ and } \tilde{\beta}_{t,n} = 0, & \text{Otherwise.} \end{cases} \tag{40}$$

4) When $a_{t,n} < 0$ and $a_{r,n} < 0$:

$$\begin{cases} \tilde{\beta}_{r,n} = -\dfrac{a_{r,n}}{2} \text{ and } \tilde{\beta}_{t,n} = -\dfrac{a_{t,n}}{2}, & \text{if } \frac{\sum_i a_{i,n}^2}{4} \le P_{\mathrm{A}}^{\max}, \\ \tilde{\beta}_{r,n} = \varsigma_{r,n} \text{ and } \tilde{\beta}_{t,n} = \varsigma_{t,n}, & \text{Otherwise,} \end{cases} \tag{41}$$

where $\varsigma_{i,n} = -\frac{a_{i,n}\sqrt{P_{\mathrm{A}}^{\max}}}{\sqrt{a_{t,n}^2 + a_{r,n}^2}}, \forall i,n$.

Proof: Please see Appendix B. ■

Algorithm 2 AO Algorithm for Solving Problem (36)

1: Input: $\{\boldsymbol{\Phi}_i\}$, $\mathbf{R}_x$, $\{\boldsymbol{w}_k\}$, $\boldsymbol{\Omega}$, $\mathbf{A}$, Z, and $\tilde{\mathbf{B}}$.
2: **repeat**
3: Update $\{\tilde{\beta}_{i,n}\}$ by (38)-(41).
4: Update $\{\tilde{\theta}_{i,n}\}$ by (43).
5: **until** the fractional reduction of the objective in (36a) falls below the predefined threshold.
6: Output: $[\tilde{\boldsymbol{\phi}}_i]_n = \tilde{\beta}_{i,n} e^{j\tilde{\theta}_{i,n}}$.

2) Optimize $\{\tilde{\theta}_{i,n}\}$: For any given $\{\tilde{\beta}_{i,n}\}$, the subproblem of optimizing $\{\tilde{\theta}_{i,n}\}$ is expressed as

$$\min_{\{\tilde{\theta}_{i,n}\}} \quad \sum_i \sum_{n=1}^{N} \mathrm{Re}\left\{ \chi_{i,n}^* \tilde{\beta}_{i,n} e^{j\tilde{\theta}_{i,n}} \right\}, \tag{42a}$$

$$\text{s.t.} \quad \left| \tilde{\theta}_{t,n} - \tilde{\theta}_{r,n} \right| = \frac{\pi}{2} \text{ or } \frac{3\pi}{2}, \quad \tilde{\theta}_{i,n} \in [0, 2\pi), \quad \forall i,n. \tag{42b}$$

Although problem (42) is non-convex arising from the non-convex constraint (42b), the optimal closed-form solution of problem (42), $\tilde{\theta}_{i,n}, \forall i,n$, is given in the following according to [10, Proposition 3]

$$\begin{cases} \tilde{\theta}_{r,n} = \dfrac{3}{2}\pi - \angle\varsigma_n \text{ and } \tilde{\theta}_{t,n} = \pi - \angle\varsigma_n \text{ or} \\ \tilde{\theta}_{r,n} = \dfrac{1}{2}\pi - \angle\bar{\varsigma}_n \text{ and } \tilde{\theta}_{t,n} = \pi - \angle\bar{\varsigma}_n, \end{cases} \tag{43}$$

where $\varsigma_n = \kappa_{t,n} + j\kappa_{r,n}$ and $\bar{\varsigma}_n = \kappa_{t,n} - j\kappa_{r,n}$ with $\kappa_{i,n} = \chi_{i,n}^* \tilde{\beta}_{i,n}, \forall i,n$. The solution is selected from one of two pairs in (43) such that the objective value in (42a) is minimized.

Based on **Proposition 2** and (43), we iteratively update the optimal closed-form solutions of problems (37) and (42), until the convergence is achieved. The details of the AO method used to solve problem (36) are provided in **Algorithm 2**.

D. Update $\tilde{\mathbf{B}}$

Based on the optimized variable $\boldsymbol{\Phi}_r$ after solving problem (34), $\tilde{\mathbf{B}}$ can be updated as follow

$$\tilde{\mathbf{B}} = |\alpha|^2 \sigma_{\mathrm{I}}^2 \left\| \boldsymbol{\Phi}_r \right\|_{\mathrm{F}}^2 \bar{\mathbf{H}} + \sigma_s^2 \mathbf{I}_{N_s}. \tag{44}$$

E. Overall Algorithm

Based on the preceding subsections, the details of the BCD method used to optimize problem (27) are presented in **Algorithm 3**. Following this, problem (27) is solved using the BCD method as described in Step 3 of **Algorithm 1**. After obtaining a solution, the optimization variables are used to evaluate constraint violations, and the penalty factor along with the Lagrangian dual variables are updated accordingly (see Steps 4–13 in **Algorithm 1**). This process is repeated until convergence is achieved (see Step 15 in **Algorithm 1**) [32]. The computational complexity associated with solving problem (27) is analyzed as follows: 1) the computational complexity of optimizing subproblem 1 is $\mathcal{O}(((K+3)^{6.5}N_t^{6.5} + N^{6.5})\log(1/\varepsilon))$ according to [10], where ε represents the solution accuracy; 2) the computational complexity of optimizing subproblem 2 is $\mathcal{O}(((K+4)^{6.5}(N+1)^{6.5})\log(1/\varepsilon))$; 3) the computational complexities of updating $\{\tilde{\beta}_{i,n}\}$ and $\{\tilde{\theta}_{i,n}\}$ are $\mathcal{O}(8N)$ and $\mathcal{O}(4N)$, respectively.

Algorithm 3 BCD Algorithm for Solving Problem (27) or (28)

1: Input: $\{\mathbf{\Phi}_i\}$, $\{\tilde{\boldsymbol{\phi}}_i\}$, $\tilde{\mathbf{B}}$, $\mathbf{\Psi}$, ψ_z, $\{\psi_i\}$, and μ.
2: **repeat**
3: Solve problem (31), and recover rank-one solution by (32).
4: Solve problem (34) for coupled phase-shift case or (45) for independent phase-shift case.
5: Solve problem (36) for coupled phase-shift case by **Algorithm 2**.
6: Update $\tilde{\mathbf{B}}^{(x+1)}$ by (44).
7: **until** the fractional reduction of the objective in (27a) falls below the predefined threshold.
8: Output: $\mathbf{R}_x$, $\mathbf{\Omega}$, $\{\mathbf{\Phi}_i\}$, Z, and $\{\tilde{\boldsymbol{\phi}}_i\}$.

V. CRB Optimization for Independent Phase-Shift Case Based on BCD Method

For the independent phase-shift case, problem (28) is decomposed into two subproblems. The solution methods for these subproblems are presented in the following subsections.

A. Optimize Beamformer at the BS

For any given $\{\mathbf{\Phi}_i\}$, $\{\tilde{\boldsymbol{\phi}}_i\}$, and $\tilde{\mathbf{B}}$, the subproblem of optimizing $\mathbf{\Delta}_w$ follows the same procedure as previously described. The corresponding rank-one solution can be recovered by (32).

B. Optimize Beamforming Matrix at the MFS

Due to the absence of auxiliary variables $\{\tilde{\boldsymbol{\phi}}_i\}$, the subproblem of optimizing the beamforming matrix $\{\mathbf{\Phi}_i\}$ for any given $\mathbf{R}_x$, $\{\boldsymbol{w}_k\}$, $\mathbf{\Omega}$, $\mathbf{A}$, Z, and $\tilde{\mathbf{B}}$, is different from the coupled phase-shift case. Specifically, by letting $\mathbf{V}_i = \boldsymbol{\phi}_i\boldsymbol{\phi}_i, \forall i$, problem (28) with respect to optimizing $\{\mathbf{\Phi}_i\}$ can be equivalently rewritten as

$$\min_{\{\mathbf{V}_i\}} \left\| \mathbf{\Omega} - \sum_{b=1}^{B} \mathbf{Q}_b \mathbf{V}_r \mathbf{Q}_b^H + \mu\mathbf{\Psi} \right\|_{\mathrm{F}}^2 + |Z - \mathrm{Tr}\left(\mathbf{V}_r\right) + \mu\psi_z|^2, \tag{45a}$$

$$\text{s.t.} \quad \tilde{\gamma}_k \mathrm{Tr}\left(\bar{\mathbf{H}}_k \mathbf{V}_t\right) \geq \mathrm{Tr}\left(\mathbf{U}_k \mathbf{V}_t^*\right) + \sigma_{\mathrm{I}}^2 \mathrm{Tr}\left(\hat{\mathbf{H}}_k \mathbf{V}_t^*\right), \quad \forall k, \tag{45b}$$

$$\begin{bmatrix} \hat{\mathbf{J}}_{\boldsymbol{\varphi}\boldsymbol{\varphi}} - \mathbf{A} & \hat{\mathbf{J}}_{\boldsymbol{\varphi}\boldsymbol{\alpha}} \\ \hat{\mathbf{J}}_{\boldsymbol{\varphi}\boldsymbol{\alpha}}^H & \hat{\mathbf{J}}_{\boldsymbol{\alpha}\boldsymbol{\alpha}} \end{bmatrix} \succeq \mathbf{0}, \tag{45c}$$

$$\sum_{b=1}^{B} \mathrm{Tr}\left(\mathbf{Q}_b \mathbf{V}_t \mathbf{Q}_b^H\right) + \mathrm{Tr}\left(\mathbf{\Omega}\right) + M \leq P_{\mathrm{R}}^{\max}, \tag{45d}$$

$$[\mathbf{V}_t]_{n,n} + [\mathbf{V}_r]_{n,n} \leq P_{\mathrm{A}}^{\max}, \quad \forall n, \tag{45e}$$

$$\mathbf{V}_i \succeq \mathbf{0}, \quad \forall i, \tag{45f}$$

$$\mathrm{Rank}\left(\mathbf{V}_i\right) = 1, \quad \forall i, \tag{45g}$$

where $\bar{\mathbf{H}}_k = \bar{\boldsymbol{h}}_k \bar{\boldsymbol{h}}_k^H$; $\hat{\mathbf{H}}_k = \mathrm{Diag}(\boldsymbol{h}_k^H)\mathrm{Diag}(\boldsymbol{h}_k)$; $\hat{\mathbf{J}}_{\boldsymbol{\varphi}\boldsymbol{\varphi}} = \bar{\mathbf{J}}_{\boldsymbol{\varphi}\boldsymbol{\varphi}} + \bar{Y}_1 \bar{\bar{\mathbf{J}}}_{\boldsymbol{\varphi}\boldsymbol{\varphi}}$, $\hat{\mathbf{J}}_{\boldsymbol{\varphi}\boldsymbol{\alpha}} = \bar{\mathbf{J}}_{\boldsymbol{\varphi}\boldsymbol{\alpha}} + \bar{Y}_2 \bar{\bar{\mathbf{J}}}_{\boldsymbol{\varphi}\boldsymbol{\alpha}}$, and $\hat{\mathbf{J}}_{\boldsymbol{\alpha}\boldsymbol{\alpha}} = \bar{\mathbf{J}}_{\boldsymbol{\alpha}\boldsymbol{\alpha}} + \bar{Y}_3 \bar{\bar{\mathbf{J}}}_{\boldsymbol{\alpha}\boldsymbol{\alpha}}$ with $\bar{Y}_1 = L|\alpha|^4\sigma_{\mathrm{I}}^4 Z\mathrm{Tr}(\mathbf{V}_r)$, $\bar{Y}_2 = 2L|\alpha|^2\sigma_{\mathrm{I}}^4 Z\mathrm{Tr}(\mathbf{V}_r)$, and $\bar{Y}_3 = 4L\sigma_{\mathrm{I}}^4 Z\mathrm{Tr}(\mathbf{V}_r)$, respectively; and $M = \sigma_{\mathrm{I}}^2 \mathrm{Tr}\left(\mathbf{V}_t + \mathbf{V}_r\right)$. Similar to problem (34), we relax the rank-one constraint in (45g), thereby making problem (45) convex and solvable using well-established optimization toolboxes [33]. If the resulting solution does not have rank one, Gaussian randomization [34] can be employed to generate a large number of rank-one candidate solutions. Among these, the solution that minimizes the objective function in (45b) is selected.

C. Update $\tilde{\mathbf{B}}$

Based on the optimized variable $\mathbf{\Phi}_r$ after solving problem (45), $\tilde{\mathbf{B}}$ can be updated using equation (44).

D. Overall Algorithm

The details of solving problem (28) within the inner loop based on BCD method are provided in **Algorithm 3**. In particular, we iteratively perform only Steps 3 and 4 and excluding Step 5 in **Algorithm 3**, until convergence is achieved, as no auxiliary variables $\{\tilde{\boldsymbol{\phi}}_i\}$ are introduced to decouple the coupling between coupled phase-shift constraint and other constraints. Similar to the case of independent phase-shift, the computational complexity of optimizing the subproblem with respect to $\mathbf{\Delta}_w$ in the coupled phase-shift scenario is $\mathcal{O}(((K+3)^{6.5}N_t^{6.5} + N^{6.5})\log(1/\varepsilon))$, while the computational complexity of optimizing $\{\mathbf{\Phi}_i\}$ is $\mathcal{O}(((K+2)^{6.5}N^{6.5})\log(1/\varepsilon))$.

VI. Simulation Results

In this section, we present numerical and simulation results to evaluate the performance of the proposed MFS-aided ISAC scheme. Specifically, we compare against the following baseline schemes:

- **Radar-Coupled/Radar-Independent:** These baselines do not impose the SINR constraint as defined in (23b). That is, the MFS is used solely for target sensing, without consideration for the communication performance of users. For the **Radar-Coupled** scheme, we optimize problem (27), whereas for the **Radar-Independent** scheme, we optimize problem (28).
- **STARS-Coupled/STARS-Independent:** [10] These baselines correspond to schemes without amplifiers at the MFS. In this setting, we have $\mathbf{P}_i = \mathbf{I}_N, \forall i$ and $\sigma_{\mathrm{I}} = 0$. As a result, the second terms in $\mathbf{J}_{\boldsymbol{\varphi}\boldsymbol{\varphi}}$, $\mathbf{J}_{\boldsymbol{\varphi}\boldsymbol{\alpha}}$, and $\mathbf{J}_{\boldsymbol{\alpha}\boldsymbol{\alpha}}$ as defined in (50), (51), and (52), respectively, are omitted, yielding a CRB matrix consistent with that in [10]. We optimize problem (27) for the **STARS-Coupled** scheme and problem (27) for the **STARS-Independent** scheme.
- **MFS-WOPH/STARS-WOPH:** In these baselines, "WOPH" means "without optimizing phase-shift matrix". Thus, the phase-shift matrix is set to $\mathbf{\Theta}_i = \sqrt{\frac{1}{2}}\mathbf{I}_N, \forall i$ following power equal division.

In addition to the above baselines, the **MFS-Coupled** and **MFS-Independent** schemes correspond to the proposed design, optimized by solving problem (27) and problem (28), respectively. Before presenting and discussing the numerical results, we define the key simulation parameters used throughout the evaluation, unless stated otherwise. The channels **G** and

$\boldsymbol{h}_k$ are modeled as Rician fading channels, a general model in which the Rician factor κ controls the propagation condition: $\kappa \to \infty$ represents a line-of-sight (LoS) environment, while $\kappa = 0$ corresponds to a non-line-of-sight (NLoS) scenario. Then, the Rician fading models of $\mathbf{G}$ and $\boldsymbol{h}_k$ are respectively given by

$$\mathbf{G} = \sqrt{\mathrm{PL}_{\mathbf{G}}}\left(\sqrt{\frac{\kappa}{1+\kappa}}\mathbf{G}^{\mathrm{LoS}} + \sqrt{\frac{1}{1+\kappa}}\mathbf{G}^{\mathrm{NLoS}}\right), \tag{46}$$

$$\boldsymbol{h}_k = \sqrt{\mathrm{PL}_k}\left(\sqrt{\frac{\kappa}{1+\kappa}}\boldsymbol{h}_k^{\mathrm{LoS}} + \sqrt{\frac{1}{1+\kappa}}\boldsymbol{h}_k^{\mathrm{NLoS}}\right), \ \forall k, \tag{47}$$

where ρ represents the path loss at the reference distance of 1 m; $\mathrm{PL}_{\mathrm{G}} = -30 - 10\zeta_{\mathbf{G}}\log_{10}(d_{\mathrm{BM}})$ dB and $\mathrm{PL}_k = -30 - 10\zeta_k \log_{10}(d_k)$ dB represent the large scale path loss for channels $\mathbf{G}$ and $\boldsymbol{h}_k$ [35], respectively, with d_{BM} and d_k being the distances between the BS and the MFS as well as the MFS and the kth user, respectively, and $\zeta_{\mathbf{G}}$ and ζ_k being the corresponding path loss exponents; $\mathbf{G}^{\mathrm{LoS}}$ and $\boldsymbol{h}_k^{\mathrm{LoS}}$ denote the LoS links for channels $\mathbf{G}$ and $\boldsymbol{h}_k$, respectively, where $\mathbf{G}^{\mathrm{LoS}}$ is constructed by multiplying steering vector of AoA with that of angle-of-derivation (AoD) for channel $\mathbf{G}$ [36], and the channel $\boldsymbol{h}_k^{\mathrm{LoS}}$ is constructed using the same method; $\mathbf{G}^{\mathrm{NLoS}}$ and $\boldsymbol{h}_k^{\mathrm{NLoS}}$ are constructed by generating a random matrix and a random vector, each entry of which follows $\mathcal{CN}(0,1)$. In this work, we set $\rho = -30$ dB, $d_{\mathrm{BM}} = 30$ m, $\kappa = 5$ dB, and $\zeta_{\mathbf{G}} = \zeta_k = 2, \forall k$ [10]. In addition, $d_k, \forall k$ is randomly generated from 20 m to 50 m. Regarding target parameters, the distance between the MFS and the target is set to $d_s = 30$ m, and the azimuth AoA φ_h and elevation AoA φ_v are set to $\varphi_h = 120°$ and $\varphi_v = 30°$. For fairness of comparisons, we set the same maximum available total power $P_{\mathrm{tot}} = 30$ dBm for the proposed scheme and **STARS** scheme, where $P_{\mathrm{tot}} = P_{\mathrm{R}}^{\max} + P_{\mathrm{BS}}^{\max}$ with $P_{\mathrm{R}}^{\max} = 0.2\ P_{\mathrm{tot}}$ for the proposed scheme and $P_{\mathrm{tot}} = P_{\mathrm{BS}}^{\max}$ for **STARS** scheme [16], [37].[6] The maximum available amplification factor is set to $P_{\mathrm{A}}^{\max} = 5$ dB. The number of elements, sensors, antennas, and users are set to $N = 5 \times 2 = 10$, $N_s = 5$, $N_t = 10$, $K = 2$, respectively. The noises are set to $\sigma_{\mathrm{I}}^2 = \sigma_u^2 = \sigma_s^2 = -110$ dBm [10]. The minimum communication SINR threshold is set to $\bar{\gamma}_1 = \ldots = \bar{\gamma}_K = 0$ dB. Finally, we set the convergence thresholds of **Algorithm 1** and **Algorithm 2** to 10^{-4}, and that of **Algorithm 3** to 10^{-3}.

A. Convergence Behavior of the Proposed Algorithm

Fig. 2 shows the convergence behavior of the proposed algorithm. Specifically, the first sub-figure in Fig. 2 depicts the convergence behavior of **Algorithm 3**, where the objective value is shown in (27a). The second and the third sub-figures in Fig. 2 depict the convergence behaviors of **Algorithm 1** with respect to constraint violation and root CRB, respectively, where the constraint violation is shown in Step 5 of **Algorithm 1**, and the root CRB is computed by $\sqrt{\mathrm{Tr}(\mathrm{CRB}_{\boldsymbol{\varphi}})}$ according to **Lemma 1**. It can observed that, the proposed algorithm converges to a stationary point with limited iterations. Specifically, in the first sub-figure of Fig. 2, the proposed algorithm converges within 8 iterations, while in the second and the third sub-figures of Fig. 2, the proposed algorithm converges within 6 iterations. This confirms the efficient and stable convergence behavior of the proposed algorithm.

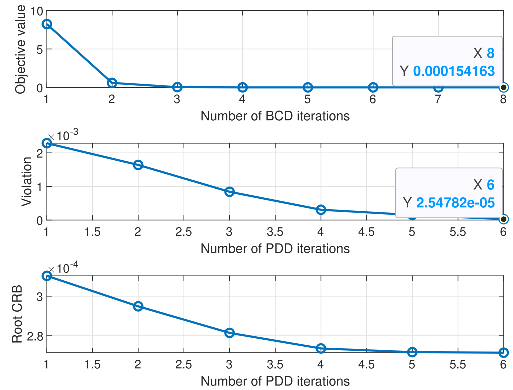

Fig. 2. Convergence behavior of the proposed algorithm.

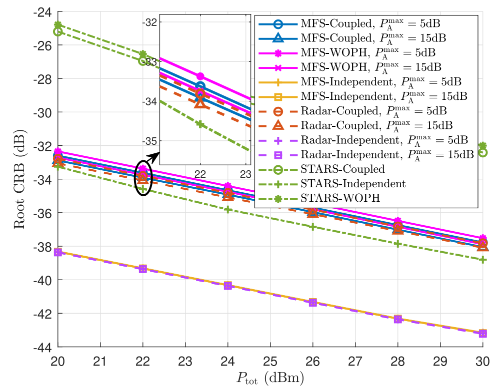

Fig. 3. Root CRB versus maximum available total power P_{tot}.

B. Impact of Maximum Available Total Power

Fig. 3 shows the root CRB versus the maximum available total power P_{tot}. We can observe that, the root CRB of all schemes decreases as P_{tot} increases, since the maximum available total power allows larger feasible region, and in this case the BS and the MFS can allocate more power for beamformer to align with the desired users and the target. In addition, as $P_{\mathrm{A}}^{\max}$ increases, the root CRBs of the **MFS-Coupled/MFS-Independent** and **Radar-Coupled/Radar-Independent** schemes improve, since a larger $P_{\mathrm{A}}^{\max}$ provides greater DoF in allocating the amplification factors. This enables the MFS beamformer to more effectively align with the target, thereby enhancing sensing performance. We can also observe that the root CRBs

[6] Due to the introduction of phase shifters and amplifiers for adjustment of phase-shift and amplification of power for incoming signals at the MFS, respectively, there is an additional hardware consumption compared to conventional RIS [7]. Specifically, the hardware consumption for the MFS is given by $2(P_{\mathrm{PH}} + P_{\mathrm{DC}})N + N_s P_s$, where P_{PH}, P_{DC} [38], and P_s represent the power consumptions of each phase shifter, direct current (DC) biasing for each amplifier, and low-cost sensing sensors [16], respectively. Since we mainly focus on the beamforming design for the CRB minimization problem in the MFS aided ISAC system, the power consumption regarding the hardware cost is ignored in this paper, as the main gap of the power consumption for different surface aided ISAC systems is signal power.

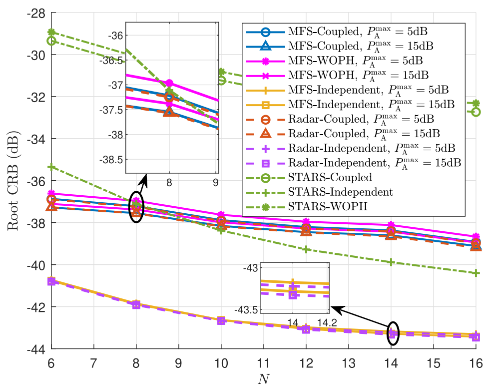

Fig. 4. Root CRB versus number of elements at the MFS, N.

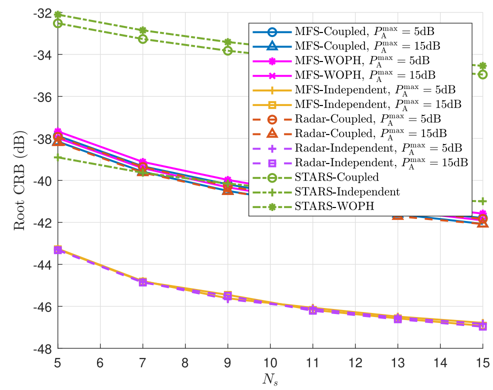

Fig. 5. Root CRB versus number of sensing sensors at the MFS, N_s.

of the **MFS-WOPH** scheme with $P_{\rm A}^{\max} = 5$ dB and $P_{\rm A}^{\max} = 15$ dB and that of the **STARS-WOPH** scheme has performance loss as compared with the case optimizing phase-shift, which demonstrates the importance of optimizing the MFS beamforming matrix, $\mathbf{\Phi}_i = \mathbf{P}_i\mathbf{\Theta}_i$ from the perspective of maximum available total power, $P_{\rm tot}$, as compared to the case that only optimizes the MFS amplification factor matrix $\mathbf{\Phi}_i = \mathbf{P}_i$. Moreover, the root CRBs of the **MFS-Independent** and **STARS-Independent** schemes are lower than those of the **MFS-Coupled** and **STARS-Coupled** schemes, respectively. However, the independent phase-shift configurations, as adopted in the **MFS-Independent** and **STARS-Independent** schemes, incur higher manufacturing costs to achieve such improved sensing performance [10], [13]. Furthermore, although the root CRBs of the **STARS-Coupled** and **STARS-Independent** schemes decrease more rapidly as $P_{\rm tot}$ increases, there remain notable performance gaps between the **MFS-Coupled/MFS-Independent** schemes and their **STARS-Coupled/STARS-Independent** counterparts. This is because the MFS actively amplifies the reflected/transmitted signal before beamforming. This amplification compensates for the severe path loss along the BS $\rightarrow$ MFS $\rightarrow$ target $\rightarrow$ sensor echo path, which undergoes double-fading. As $P_{\rm tot}$ increases, MFS can allocate more power to amplification, further boosting the echo SNR at the embedded sensors, whereas STARS is fundamentally limited by its passive nature and cannot exploit the additional power budget in the same way. This clearly demonstrates the substantial potential of deploying MFS in ISAC systems, offering superior sensing performance compared to STARS-based solutions.

C. Impact of Number of Elements at the MFS

Fig. 4 shows the root CRB versus the number of elements at the MFS, N. We can also find that, the schemes without optimizing phase-shift, that is, the scheme of **MFS-WOPH** with $P_{\rm A}^{\max} = 5$ dB and $P_{\rm A}^{\max} = 15$ dB and that of **STARS-WOPH** decreases with the increasing of number of elements, but both of these two schemes suffer from performance degradation in terms of CRB from the perspective of number of elements at the MFS. This means that we need to incorporate phase-shift matrix into the optimization for avoiding CRB degradation. We can also find that, the root CRB of all schemes decreases with the increasing of N. This is because the increasing of number of elements at the MFS increases the number of controllable links brought by the MFS, resulting in more transmitting and reflecting links for better serving communication users and the target. Additionally, a higher maximum available amplifier power $P_{\rm A}^{\max}$ leads to greater improvements in sensing performance for the **MFS-Coupled/MFS-Independent** and **Radar-Coupled/Radar-Independent** schemes, compared to deploying STARS for ISAC functionality. The performance gain from increasing N is more pronounced for MFS than STARS. This is because each additional MFS element contributes not only an extra controllable propagation path but also an additional amplification degree of freedom. Specifically, with N elements, the MFS can coherently amplify and steer N independent signal components toward the target, resulting in an array gain that scales more favorably than the passive beamforming gain of STARS.

D. Impact of Number of Sensors at the MFS

Fig. 5 illustrates the root CRB as a function of the number of sensors N_s at the MFS. It can also be observed that the root CRB of all schemes decreases as N_s increases. This is because a larger number of sensors introduces more controllable links, thereby enhancing the number of echo paths for improved target sensing. Moreover, the performance gaps between the **MFS-Coupled/MFS-Independent** schemes and **STARS-Coupled/STARS-Independent** baselines remain significant. The persistent performance gap between MFS and STARS as N_s grows can be attributed to the signal quality at each sensor. With STARS, the echo signal arriving at each sensor has already suffered double-path loss without any compensation, so adding more sensors primarily averages weak signals. With MFS, the amplified echo signal carries higher SNR per sensor, meaning each additional sensor contributes a more informative observation to the FIM. This further confirms the advantage of deploying MFS in ISAC systems, especially as the number of sensors increases.

E. Impact of Minimum Communication SINR Threshold

Fig. 6 illustrates the root CRB as a function of the minimum communication SINR threshold, $\bar{\gamma}_k$. It can be observed that as $\bar{\gamma}_k$ increases, the root CRB increases for all schemes, except

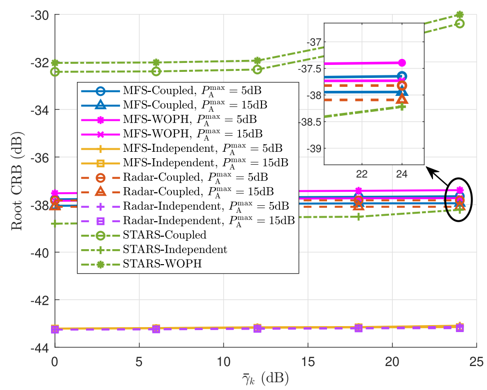

Fig. 6. Root CRB versus minimum communication SINR threshold, $\bar{\gamma}_k$.

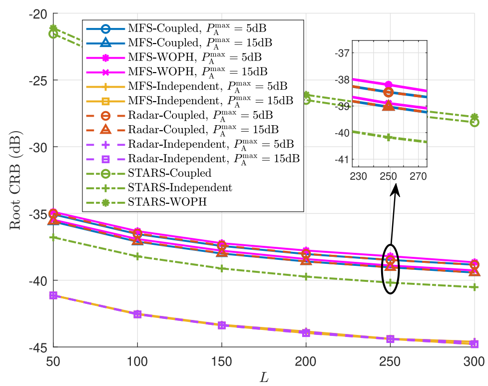

Fig. 7. Root CRB versus number of sensing blocks, L.

for the **Radar-Coupled** and **Radar-Independent** schemes. This is because a higher SINR threshold requires more beamforming power to be allocated to communication users in order to satisfy stricter quality-of-service demands. Consequently, less power is available for sensing, which leads to a degradation in sensing performance, reflected by the increased root CRB. The **Radar-Coupled** and **Radar-Independent** schemes remain unaffected because they are designed solely for sensing and do not impose communication constraints. In addition, the root CRB gaps between **MFS-Coupled/MFS-Independent** and **Radar-Coupled/Radar-Independent** increase as $\bar{\gamma}_k$ increases, with the root CRB of **Radar-Coupled/Radar-Independent** remaining unchanged. This is because the **Radar-Coupled/Radar-Independent** scheme is not affected by the communication metric $\bar{\gamma}_k$.

F. Impact of Number of Sensing Blocks

Fig. 7 shows root CRB versus the number of sensing blocks, L. It can be observed that the root CRB of all schemes decreases as L increases, demonstrating the improved sensing performance when the number of sensing blocks increases. Specifically, the increased number of blocks allows more time for sensing function, resulting in progressive increase for receiving sensing echo signal. Additionally, the proposed scheme with the help of an MFS is superior to the scheme with the help of an STARS, regardless of whether the phase-shift is coupled or independent. These discussions demonstrate the superiority of introducing MFS in ISAC systems in terms of CRB.

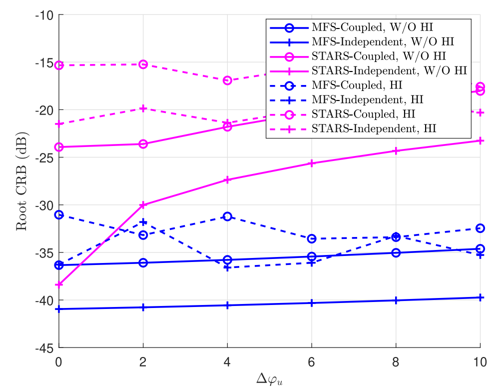

Fig. 8. Root CRB versus angle estimation error level, $\Delta\varphi_u$.

G. Impact of AoA Estimation Error and Hardware Impairment

In this work, the perfect CSI of sensing links including the parameters of AoA is assumed. To investigate the robustness performance of the proposed scheme with the aid of an MFS, we present Fig. 8. Specifically, in Fig. 8, "HI" and "W/O HI" represent the MFS or STARS with and without hardware impairment, respectively. We first discuss the AoA estimation error and hardware impairment models in the following. According to [39], the estimation uncertainty model of the estimated angle for the target can be expressed as $\varphi_u = \hat{\varphi}_u + \Delta\varphi_u$, where $\hat{\varphi}_u, u \in \{h, v\}$ denotes the estimated angle, and $\Delta\varphi_u$ denotes the corresponding AoA estimation error. In addition, the impact of hardware impairment at the MFS on the received signal at the users and the target can be modeled by inserting a random diagonal phase noise matrix, $\tilde{\mathbf{\Theta}}_i, \forall i \in \{r, t\}$, where each diagonal element $[\tilde{\mathbf{\Theta}}_i]_{n,n} = e^{j\vartheta_n^i}$ with ϑ_n^i representing the phase noise caused by hardware impairment at the MFS and following uniform distribution within $[-\pi/2, \pi/2]$ [40], so that the received signal at the kth user and the target are respectively given by

$$\boldsymbol{y}_k^T = \boldsymbol{h}_k^H \tilde{\mathbf{\Phi}}_t \mathbf{G}\mathbf{X} + \boldsymbol{h}_k^H \tilde{\mathbf{\Phi}}_t \mathbf{N}_{\rm I} + \boldsymbol{n}_{\rm u}^T, \tag{48}$$

$$\boldsymbol{y}_r^l = \tilde{\mathbf{H}} \tilde{\mathbf{\Phi}}_r \mathbf{G}\boldsymbol{x}_l + \tilde{\mathbf{H}} \tilde{\mathbf{\Phi}}_r \boldsymbol{n}_{\rm I}^l + \boldsymbol{n}_s^l, \tag{49}$$

where $\tilde{\mathbf{\Phi}}_i = \mathbf{\Phi}_i \tilde{\mathbf{\Theta}}_i$. Based on the above, Fig. 8 shows the root CRB versus angle estimation error level under the case with and without hardware impairment. It can be seen from Fig. 8 that, the root CRB of all schemes increases as the CSI uncertainty level increases. This reflects the mismatch of the beamforming design between the perfect AoA estimation and the imperfect AoA estimation. In the case without hardware impairment, the STARS scheme incur a 24.63% and 39.43% performance losses for the coupled phase-shift and the independent phase-shift architectures, respectively, when the AoA estimation error is $\Delta\varphi_u = 10°, \forall u \in \{h, v\}$, as compared with the case with perfect AoA estimation. Fortunately, when the AoA estimation is $\Delta\varphi_u = 10°, \forall u \in \{h, v\}$, the proposed MFS scheme only has 4.73% and 2.96% performance losses for the coupled phase-shift and independent phase-shift architectures, respectively. When the assumed AoA deviates from the true value, the beamforming matrix $\mathbf{\Phi}_r$ is no longer perfectly aligned with the target direction, causing a beamforming gain loss. In other words, MFS trades some amplification power for robustness against steering errors. This means that the proposed MFS scheme presents a stronger robustness to AoA estimation error. Moreover, the impact of hardware impairment is shown in dashed lines as shown in Fig. 8. We can observe that, although the hardware impairment degrades the root CRB value of all schemes, the proposed independent/coupled phase-shift MFS scheme outperforms the STARS scheme, which demonstrates the superiority of the proposed MFS scheme.

VII. Conclusion

In this work, we proposed an MFS to enhance ISAC. In the proposed scheme, the BS transmits the ISAC signal to the MFS, which amplifies the incoming signal and then performs simultaneous transmission and reflection, serving communication users and the sensing target, respectively. To evaluate sensing performance, we derived a closed-form CRB that accounts for the dynamic noise introduced by the amplifiers at the MFS–a key distinction from existing CRB formulations used in other ISAC systems. Furthermore, we developed efficient optimization methods to minimize the CRB under a variety of practical constraints, for both coupled and independent phase-shift configurations. Simulation results demonstrated that the proposed scheme outperforms existing baselines, including recently studied approaches based on STARS.

For the future work of this paper, the extension of the MFS, multi-functional topological metasurfaces [41], [42], having modular and programmable meta-atoms and the capability of manipulating surface and space electromagnetic waves, is expected to deploy in the ISAC system, as compared to the proposed MFS which manipulates electromagnetic wave, and in this way the topological surface for controlling the surface waves will be studied in the future. In addition, the broader performance metrics, e.g., achievable rage, latency, energy efficiency, detection probability, and false alarm probability will be investigated in our future work.

$$
\begin{aligned}
\mathbf{J}_{\boldsymbol{\varphi}\boldsymbol{\varphi}} &= 2\mathrm{Re}\left\{\frac{\partial \boldsymbol{u}^H}{\partial \boldsymbol{\varphi}}\left(\mathbf{I}_L\otimes\tilde{\mathbf{B}}^{-1}\right)\frac{\partial \boldsymbol{u}}{\partial \boldsymbol{\varphi}}\right\} + \mathrm{Tr}\left(\left(\mathbf{I}_L\otimes\tilde{\mathbf{B}}^{-1}\right)\frac{\partial \mathbf{C}}{\partial \boldsymbol{\varphi}}\left(\mathbf{I}_L\otimes\tilde{\mathbf{B}}^{-1}\right)\frac{\partial \mathbf{C}}{\partial \boldsymbol{\varphi}}\right)\\
&= 2\mathrm{Re}\left\{\begin{bmatrix}\mathrm{vec}^H\left(\alpha\dot{\mathbf{H}}_{\varphi_h}\boldsymbol{\Phi}_r\mathbf{G}\mathbf{X}\right)\\ \mathrm{vec}^H\left(\alpha\dot{\mathbf{H}}_{\varphi_v}\boldsymbol{\Phi}_r\mathbf{G}\mathbf{X}\right)\end{bmatrix}\left(\mathbf{I}_L\otimes\tilde{\mathbf{B}}^{-1}\right)\left[\mathrm{vec}\left(\alpha\dot{\mathbf{H}}_{\varphi_h}\boldsymbol{\Phi}_r\mathbf{G}\mathbf{X}\right)\ \mathrm{vec}\left(\alpha\dot{\mathbf{H}}_{\varphi_v}\boldsymbol{\Phi}_r\mathbf{G}\mathbf{X}\right)\right]\right\}\\
&\quad + \mathrm{Tr}\left(\left(\mathbf{I}_L\otimes\tilde{\mathbf{B}}^{-1}\right)\frac{\partial \mathbf{C}}{\partial \boldsymbol{\varphi}}\left(\mathbf{I}_L\otimes\tilde{\mathbf{B}}^{-1}\right)\frac{\partial \mathbf{C}}{\partial \boldsymbol{\varphi}}\right)\\
&= 2\left|\alpha\right|^2 L\mathrm{Re}\left\{\begin{bmatrix}\mathrm{Tr}\left(\tilde{\mathbf{B}}^{-1}\dot{\mathbf{H}}_{\varphi_h}\boldsymbol{\Phi}_r\mathbf{G}\mathbf{R}_x\mathbf{G}^H\boldsymbol{\Phi}_r^H\dot{\mathbf{H}}_{\varphi_h}^H\right) & \mathrm{Tr}\left(\tilde{\mathbf{B}}^{-1}\dot{\mathbf{H}}_{\varphi_v}\boldsymbol{\Phi}_r\mathbf{G}\mathbf{R}_x\mathbf{G}^H\boldsymbol{\Phi}_r^H\dot{\mathbf{H}}_{\varphi_h}^H\right)\\ \mathrm{Tr}\left(\tilde{\mathbf{B}}^{-1}\dot{\mathbf{H}}_{\varphi_h}\boldsymbol{\Phi}_r\mathbf{G}\mathbf{R}_x\mathbf{G}^H\boldsymbol{\Phi}_r^H\dot{\mathbf{H}}_{\varphi_v}^H\right) & \mathrm{Tr}\left(\tilde{\mathbf{B}}^{-1}\dot{\mathbf{H}}_{\varphi_v}\boldsymbol{\Phi}_r\mathbf{G}\mathbf{R}_x\mathbf{G}^H\boldsymbol{\Phi}_r^H\dot{\mathbf{H}}_{\varphi_v}^H\right)\end{bmatrix}\right\}\\
&\quad + L\left|\alpha\right|^4\sigma_{\mathrm{I}}^4\left\|\boldsymbol{\Phi}_r\right\|_{\mathrm{F}}^4\begin{bmatrix}\mathrm{Tr}\left(\tilde{\mathbf{B}}^{-1}\dot{\bar{\mathbf{H}}}_{\varphi_h}\tilde{\mathbf{B}}^{-1}\dot{\bar{\mathbf{H}}}_{\varphi_h}\right) & \mathrm{Tr}\left(\tilde{\mathbf{B}}^{-1}\dot{\bar{\mathbf{H}}}_{\varphi_h}\tilde{\mathbf{B}}^{-1}\dot{\bar{\mathbf{H}}}_{\varphi_v}\right)\\ \mathrm{Tr}\left(\tilde{\mathbf{B}}^{-1}\dot{\bar{\mathbf{H}}}_{\varphi_v}\tilde{\mathbf{B}}^{-1}\dot{\bar{\mathbf{H}}}_{\varphi_h}\right) & \mathrm{Tr}\left(\tilde{\mathbf{B}}^{-1}\dot{\bar{\mathbf{H}}}_{\varphi_v}\tilde{\mathbf{B}}^{-1}\dot{\bar{\mathbf{H}}}_{\varphi_v}\right)\end{bmatrix},
\end{aligned}
\tag{50}
$$

$$
\begin{aligned}
\mathbf{J}_{\boldsymbol{\varphi}\boldsymbol{\alpha}} &= 2\mathrm{Re}\left\{\frac{\partial \boldsymbol{u}^H}{\partial \boldsymbol{\varphi}}\left(\mathbf{I}_L\otimes\tilde{\mathbf{B}}^{-1}\right)\frac{\partial \boldsymbol{u}}{\partial \boldsymbol{\alpha}}\right\} + \mathrm{Tr}\left(\left(\mathbf{I}_L\otimes\tilde{\mathbf{B}}^{-1}\right)\frac{\partial \mathbf{C}}{\partial \boldsymbol{\varphi}}\left(\mathbf{I}_L\otimes\tilde{\mathbf{B}}^{-1}\right)\frac{\partial \mathbf{C}}{\partial \boldsymbol{\alpha}}\right)\\
&= 2L\mathrm{Re}\left\{\begin{bmatrix}\mathrm{Tr}\left(\alpha^*\tilde{\mathbf{B}}^{-1}\mathbf{H}\boldsymbol{\Phi}_r\mathbf{G}\mathbf{R}_x\mathbf{G}^H\boldsymbol{\Phi}_r^H\dot{\mathbf{H}}_{\varphi_h}^H\right) & j\mathrm{Tr}\left(\alpha^*\tilde{\mathbf{B}}^{-1}\mathbf{H}\boldsymbol{\Phi}_r\mathbf{G}\mathbf{R}_x\mathbf{G}^H\boldsymbol{\Phi}_r^H\dot{\mathbf{H}}_{\varphi_h}^H\right)\\ \mathrm{Tr}\left(\alpha^*\tilde{\mathbf{B}}^{-1}\mathbf{H}\boldsymbol{\Phi}_r\mathbf{G}\mathbf{R}_x\mathbf{G}^H\boldsymbol{\Phi}_r^H\dot{\mathbf{H}}_{\varphi_v}^H\right) & j\mathrm{Tr}\left(\alpha^*\tilde{\mathbf{B}}^{-1}\mathbf{H}\boldsymbol{\Phi}_r\mathbf{G}\mathbf{R}_x\mathbf{G}^H\boldsymbol{\Phi}_r^H\dot{\mathbf{H}}_{\varphi_v}^H\right)\end{bmatrix}\right\}\\
&\quad + 2L\left|\alpha\right|^2\sigma_{\mathrm{I}}^4\left\|\boldsymbol{\Phi}_r\right\|_{\mathrm{F}}^4\begin{bmatrix}\alpha_{\mathrm{R}}\mathrm{Tr}\left(\tilde{\mathbf{B}}^{-1}\dot{\bar{\mathbf{H}}}_{\varphi_h}\tilde{\mathbf{B}}^{-1}\bar{\mathbf{H}}\right) & \alpha_{\mathrm{S}}\mathrm{Tr}\left(\tilde{\mathbf{B}}^{-1}\dot{\bar{\mathbf{H}}}_{\varphi_h}\tilde{\mathbf{B}}^{-1}\bar{\mathbf{H}}\right)\\ \alpha_{\mathrm{R}}\mathrm{Tr}\left(\tilde{\mathbf{B}}^{-1}\dot{\bar{\mathbf{H}}}_{\varphi_v}\tilde{\mathbf{B}}^{-1}\bar{\mathbf{H}}\right) & \alpha_{\mathrm{S}}\mathrm{Tr}\left(\tilde{\mathbf{B}}^{-1}\dot{\bar{\mathbf{H}}}_{\varphi_v}\tilde{\mathbf{B}}^{-1}\bar{\mathbf{H}}\right)\end{bmatrix},
\end{aligned}
\tag{51}
$$

$$
\begin{aligned}
\mathbf{J}_{\boldsymbol{\alpha}\boldsymbol{\alpha}} &= 2\mathrm{Re}\left\{\frac{\partial \boldsymbol{u}^H}{\partial \boldsymbol{\alpha}}\left(\mathbf{I}_L\otimes\tilde{\mathbf{B}}^{-1}\right)\frac{\partial \boldsymbol{u}}{\partial \boldsymbol{\alpha}}\right\} + \mathrm{Tr}\left(\left(\mathbf{I}_L\otimes\tilde{\mathbf{B}}^{-1}\right)\frac{\partial \mathbf{C}}{\partial \boldsymbol{\alpha}}\left(\mathbf{I}_L\otimes\tilde{\mathbf{B}}^{-1}\right)\frac{\partial \mathbf{C}}{\partial \boldsymbol{\alpha}}\right)\\
&= 2\mathrm{Re}\left\{\begin{bmatrix}1\\ -j\end{bmatrix}\mathrm{vec}^H\left(\mathbf{H}\boldsymbol{\Phi}_r\mathbf{G}\mathbf{X}\right)\left(\mathbf{I}_L\otimes\tilde{\mathbf{B}}^{-1}\right)\mathrm{vec}\left(\mathbf{H}\boldsymbol{\Phi}_r\mathbf{G}\mathbf{X}\right)\left[1\ j\right]\right\} + \mathrm{Tr}\left(\left(\mathbf{I}_L\otimes\tilde{\mathbf{B}}^{-1}\right)\frac{\partial \mathbf{C}}{\partial \boldsymbol{\alpha}}\left(\mathbf{I}_L\otimes\tilde{\mathbf{B}}^{-1}\right)\frac{\partial \mathbf{C}}{\partial \boldsymbol{\alpha}}\right)\\
&= 2L\mathrm{Tr}\left(\tilde{\mathbf{B}}^{-1}\mathbf{H}\boldsymbol{\Phi}_r\mathbf{G}\mathbf{R}_x\mathbf{G}^H\boldsymbol{\Phi}_r^H\mathbf{H}^H\right)\mathbf{I}_2 + 4L\sigma_{\mathrm{I}}^4\left\|\boldsymbol{\Phi}_r\right\|_{\mathrm{F}}^4\begin{bmatrix}\alpha_{\mathrm{R}}^2\mathrm{Tr}\left(\tilde{\mathbf{B}}^{-1}\bar{\mathbf{H}}\tilde{\mathbf{B}}^{-1}\bar{\mathbf{H}}\right) & \alpha_{\mathrm{R}}\alpha_{\mathrm{S}}\mathrm{Tr}\left(\tilde{\mathbf{B}}^{-1}\bar{\mathbf{H}}\tilde{\mathbf{B}}^{-1}\bar{\mathbf{H}}\right)\\ \alpha_{\mathrm{R}}\alpha_{\mathrm{S}}\mathrm{Tr}\left(\tilde{\mathbf{B}}^{-1}\bar{\mathbf{H}}\tilde{\mathbf{B}}^{-1}\bar{\mathbf{H}}\right) & \alpha_{\mathrm{S}}^2\mathrm{Tr}\left(\tilde{\mathbf{B}}^{-1}\bar{\mathbf{H}}\tilde{\mathbf{B}}^{-1}\bar{\mathbf{H}}\right)\end{bmatrix}.
\end{aligned}
\tag{52}
$$

APPENDIX A
PROOF OF LEMMA 1

First, by vectoring $\mathbf{Y}_r$ in (19) as $\bar{\boldsymbol{y}}_r$, we have

$$\underbrace{\mathrm{vec}\left(\mathbf{Y}_r\right)}_{\bar{\boldsymbol{y}}_r}=\underbrace{\mathrm{vec}\left(\tilde{\mathbf{H}}\mathbf{\Phi}_r\mathbf{G}\mathbf{X}\right)}_{\boldsymbol{u}}+\underbrace{\mathrm{vec}\left(\tilde{\mathbf{H}}\mathbf{\Phi}_r\mathbf{N}_{\mathrm{I}}\right)}_{\bar{\boldsymbol{n}}_{\mathrm{I}}}+\underbrace{\mathrm{vec}\left(\mathbf{N}_s\right)}_{\bar{\boldsymbol{n}}_s}. \tag{53}$$

Then, by conditioning $\boldsymbol{\zeta}$, we have $\bar{\boldsymbol{y}}_r\sim\mathcal{CN}\left(\boldsymbol{u},\mathbf{C}\right)$. Based on [30], each element in (21) can be obtained by $[\mathbf{F}]_{u,w}=2\mathrm{Re}\left\{\frac{\partial\boldsymbol{u}^H}{\partial\zeta_u}\mathbf{C}^{-1}\frac{\partial\boldsymbol{u}}{\partial\zeta_w}\right\}+\mathrm{Tr}\left(\mathbf{C}^{-1}\frac{\partial\mathbf{C}}{\partial\zeta_u}\mathbf{C}^{-1}\frac{\partial\mathbf{C}}{\partial\zeta_w}\right)$. To obtain the covariance matrix $\mathbf{C}$, we need to acquire the covariance matrix of $\bar{\boldsymbol{n}}_{\mathrm{I}}+\bar{\boldsymbol{n}}_s$, which is given by $\mathbf{C}=\mathbb{E}\left\{\bar{\boldsymbol{n}}_{\mathrm{I}}\bar{\boldsymbol{n}}_{\mathrm{I}}^H\right\}+\mathbb{E}\left\{\bar{\boldsymbol{n}}_s\bar{\boldsymbol{n}}_s^H\right\}=\mathbf{I}_L\otimes\tilde{\mathbf{B}}$, where $\tilde{\mathbf{B}}=\sigma_{\mathrm{I}}^2\mathbf{B}\mathbf{B}^H+\sigma_s^2\mathbf{I}_{N_s}=|\alpha|^2\sigma_{\mathrm{I}}^2\left\|\mathbf{\Phi}_r\right\|_{\mathrm{F}}^2\bar{\mathbf{H}}+\sigma_s^2\mathbf{I}_{N_s}$ with $\mathbf{B}=\tilde{\mathbf{H}}\mathbf{\Phi}_r$ and $\bar{\mathbf{H}}=\bar{\boldsymbol{h}}_r\bar{\boldsymbol{h}}_r^H$. The derivatives $\frac{\partial\boldsymbol{u}}{\partial\varphi_p}$, $\frac{\partial\mathbf{C}}{\partial\varphi_p}$, $\frac{\partial\boldsymbol{u}}{\partial\boldsymbol{\alpha}}$, and $\frac{\partial\mathbf{C}}{\partial\alpha_q},\forall p\in\{h,v\},\forall q\in\{\mathrm{R},\mathrm{S}\}$ are given by

$$\begin{aligned}
\frac{\partial\boldsymbol{u}}{\partial\varphi_p}&=\mathrm{vec}\left(\alpha\dot{\mathbf{H}}_{\varphi_p}\mathbf{\Phi}_r\mathbf{G}\mathbf{X}\right),\ \frac{\partial\mathbf{C}}{\partial\varphi_p}=\mathbf{I}_L\otimes|\alpha|^2\sigma_{\mathrm{I}}^2\left\|\mathbf{\Phi}_r\right\|_{\mathrm{F}}^2\dot{\bar{\mathbf{H}}}_{\varphi_p},\\
\frac{\partial\boldsymbol{u}}{\partial\boldsymbol{\alpha}}&=\mathrm{vec}\left(\mathbf{H}\mathbf{\Phi}_r\mathbf{G}\mathbf{X}\right)[1,j],\ \frac{\partial\mathbf{C}}{\partial\alpha_q}=\mathbf{I}_L\otimes2\alpha_q\sigma_{\mathrm{I}}^2\left\|\mathbf{\Phi}_r\right\|_{\mathrm{F}}^2\bar{\mathbf{H}},
\end{aligned}\tag{54}$$

where

$$\begin{aligned}
\dot{\mathbf{H}}_{\varphi_h}&=j\frac{2\pi}{\lambda}\sin\varphi_h\sin\varphi_v\left(\mathrm{Diag}\left(\bar{\boldsymbol{d}}_x\right)\mathbf{H}+\mathbf{H}\mathrm{Diag}\left(\boldsymbol{d}_x\right)\right),\\
\dot{\mathbf{H}}_{\varphi_v}&=-j\frac{2\pi}{\lambda}\cos\varphi_h\cos\varphi_v\left(\mathrm{Diag}\left(\bar{\boldsymbol{d}}_x\right)\mathbf{H}+\mathbf{H}\mathrm{Diag}\left(\boldsymbol{d}_x\right)\right)\\
&\quad+j\frac{2\pi}{\lambda}\sin\varphi_v\left(\mathrm{Diag}\left(\bar{\boldsymbol{d}}_z\right)\mathbf{H}+\mathbf{H}\mathrm{Diag}\left(\boldsymbol{d}_z\right)\right),\\
\dot{\bar{\mathbf{H}}}_{\varphi_h}&=j\frac{2\pi}{\lambda}\sin\varphi_h\sin\varphi_v\left(\mathrm{Diag}\left(\bar{\boldsymbol{d}}_x\right)\bar{\mathbf{H}}+\bar{\mathbf{H}}\mathrm{Diag}\left(\bar{\boldsymbol{d}}_x\right)\right),\\
\dot{\bar{\mathbf{H}}}_{\varphi_v}&=-j\frac{2\pi}{\lambda}\cos\varphi_h\cos\varphi_v\left(\mathrm{Diag}\left(\bar{\boldsymbol{d}}_x\right)\bar{\mathbf{H}}+\bar{\mathbf{H}}\mathrm{Diag}\left(\bar{\boldsymbol{d}}_x\right)\right)\\
&\quad+j\frac{2\pi}{\lambda}\sin\varphi_v\left(\mathrm{Diag}\left(\bar{\boldsymbol{d}}_z\right)\bar{\mathbf{H}}+\bar{\mathbf{H}}\mathrm{Diag}\left(\bar{\boldsymbol{d}}_z\right)\right).
\end{aligned}$$

With (54), $\mathbf{J}_{\varphi\varphi}$, $\mathbf{J}_{\varphi\alpha}$, and $\mathbf{J}_{\alpha\alpha}$ can be obtained, which are respectively given in (50)-(52) which completes the proof.

APPENDIX B
PROOF OF PROPOSITION 2

First, we can observe that problem (37) can be divided into N subproblems that can be optimized in parallel as follow

$$\min_{\{\tilde{\beta}_{i,n}\}}\quad\sum_i\left(\tilde{\beta}_{i,n}^2+a_{i,n}\tilde{\beta}_{i,n}\right), \tag{55a}$$
$$\text{s.t.}\quad\tilde{\beta}_{t,n}^2+\tilde{\beta}_{r,n}^2\le P_{\mathrm{A}}^{\max},\quad\tilde{\beta}_{i,n}\ge0,\quad\forall i. \tag{55b}$$

From a geometric point of view, problem (55) is a quarter circle projection problem. Consequently, we discuss the closed-form solution of problem (55) in the following four cases.

1) *$a_{t,n}\ge0$ and $a_{r,n}\ge0$:* In this case, it can be readily seen that the minimum of (55a) is zero, since all variables in (55a) are larger than or equal to zero. Therefore, we can easily obtain that $\tilde{\beta}_{i,n}=0$ to achieve minimum of the objective.
2) *$a_{t,n}<0$ and $a_{r,n}\ge0$:* In this case, similar to the previous case, $\tilde{\beta}_{r,n}$ needs to be set to zero to achieve the minimum of $\tilde{\beta}_{r,n}^2+a_{r,n}\tilde{\beta}_{r,n}$, such that $\tilde{\beta}_{r,n}^2+a_{r,n}\tilde{\beta}_{r,n}=0$. Therefore, problem (55) for the case of $a_{r,n}=0$ is reformulated as in the following

$$\min_{\{\tilde{\beta}_{t,n}\}}\quad\tilde{\beta}_{t,n}^2+a_{t,n}\tilde{\beta}_{t,n}, \tag{56a}$$
$$\text{s.t.}\quad\tilde{\beta}_{t,n}^2\le P_{\mathrm{A}}^{\max}. \tag{56b}$$

Then, we can use Lagrange multiplier method to obtain the optimal closed-form solution of $\{\tilde{\beta}_{t,n}\}$ for convex problem in (56). Specifically, the Lagrangian of problem (56) is given by

$$\bar{\mathcal{L}}\left(\tilde{\beta}_{t,n},\lambda_n\right)=\tilde{\beta}_{t,n}^2+a_{t,n}\tilde{\beta}_{t,n}+\lambda_n\left(\tilde{\beta}_{t,n}^2-P_{\mathrm{A}}^{\max}\right), \tag{57}$$

where λ_n represents the Lagrange multiplier. Then, the Karush–Kuhn–Tucker (KKT) conditions of problem (56) is [43]

$$\begin{aligned}
&\text{K1: }\frac{\partial\bar{\mathcal{L}}}{\partial\tilde{\beta}_{t,n}}=2\tilde{\beta}_{t,n}^{\mathrm{op}}+a_{t,n}+2\lambda_n^{\mathrm{op}}\tilde{\beta}_{t,n}^{\mathrm{op}}=0,\\
&\text{K2: }\left(\tilde{\beta}_{t,n}^{\mathrm{op}}\right)^2\le P_{\mathrm{A}}^{\max},\quad\text{K3: }\lambda_n^{\mathrm{op}}\ge0,\\
&\text{K4: }\lambda_n^{\mathrm{op}}\left(\left(\tilde{\beta}_{t,n}^{\mathrm{op}}\right)^2-P_{\mathrm{A}}^{\max}\right)=0,
\end{aligned}\tag{58}$$

where $\{\cdot\}^{\mathrm{op}}$ denotes the optimum. Note that in the KKT condition K4, if $\lambda_n^{\mathrm{op}}>0$, we have $\tilde{\beta}_{t,n}^{\mathrm{op}}=\sqrt{P_{\mathrm{A}}^{\max}}$. Substituting $\tilde{\beta}_{t,n}^{\mathrm{op}}=\sqrt{P_{\mathrm{A}}^{\max}}$ into KKT condition K1 yields $\lambda_n^{\mathrm{op}}=-\left(1+\frac{a_{t,n}}{2\sqrt{P_{\mathrm{A}}^{\max}}}\right)$. Since $a_{t,n}<0$, there are two specific cases to obtain $\tilde{\beta}_{t,n}^{\mathrm{op}}$: a) If $1\ge|\frac{a_{t,n}}{2\sqrt{P_{\mathrm{A}}^{\max}}}|$, then $\lambda_n^{\mathrm{op}}>0$ does not hold, which implies that $\lambda_n^{\mathrm{op}}=0$ according to KKT condition K3, and thus $\tilde{\beta}_{t,n}^{\mathrm{op}}=-\frac{a_{t,n}}{2}$ by letting $\lambda_n^{\mathrm{op}}=0$ in the KKT condition K1; b) if $1<|\frac{a_{t,n}}{2\sqrt{P_{\mathrm{A}}^{\max}}}|$, then $\lambda_n^{\mathrm{op}}>0$, and thus we have $\tilde{\beta}_{t,n}^{\mathrm{op}}=\sqrt{P_{\mathrm{A}}^{\max}}$ according to KKT condition K4.
3) *$a_{t,n}\ge0$ and $a_{r,n}<0$:* In this case, the optimal closed-form solution can be easily derived using the same method as for the previous case ($a_{t,n}<0$ and $a_{r,n}\ge0$).
4) *$a_{t,n}<0$ and $a_{r,n}<0$:* In this case, we can first obtain the closed-form solutions for unconstrained version of problem (55), which are given by $\tilde{\beta}_{r,n}=\bar{\tilde{\beta}}_{r,n}=-\frac{a_{r,n}}{2}$ and $\tilde{\beta}_{t,n}=\bar{\tilde{\beta}}_{t,n}=-\frac{a_{t,n}}{2}$. Based on this, if $\bar{\tilde{\beta}}_{r,n}^2+\bar{\tilde{\beta}}_{t,n}^2=\frac{a_{r,n}^2+a_{t,n}^2}{4}\le P_{\mathrm{A}}^{\max}$, $\bar{\tilde{\beta}}_{r,n}$ and $\bar{\tilde{\beta}}_{t,n}$ are the optimal closed-form solutions for problem (55). On the other hand, if $\bar{\tilde{\beta}}_{r,n}+\bar{\tilde{\beta}}_{t,n}>P_{\mathrm{A}}^{\max}$, we can use Lagrange multiplier method to obtain the optimal closed-form solution. Specifically, the Lagrangian of problem (55) is given by

$$\begin{aligned}
\tilde{\mathcal{L}}\left(\tilde{\beta}_{r,n},\tilde{\beta}_{t,n},\lambda_n\right)&=\tilde{\beta}_{r,n}^2+\tilde{\beta}_{t,n}^2+a_{r,n}\tilde{\beta}_{r,n}+a_{t,n}\tilde{\beta}_{t,n}\\
&\quad+\tilde{\lambda}_n\left(\tilde{\beta}_{r,n}^2+\tilde{\beta}_{t,n}^2-P_{\mathrm{A}}^{\max}\right),
\end{aligned}\tag{59}$$

where $\tilde{\lambda}_n$ represents the Lagrange multiplier. Then, the KKT conditions of problem (55) is [43]

$$\widetilde{\mathrm{K1}}: \ \frac{\partial \tilde{\mathcal{L}}}{\partial \tilde{\beta}_{i,n}} = a_{i,n} + 2\tilde{\lambda}_n^{\mathrm{op}} \tilde{\beta}_{i,n}^{\mathrm{op}} = 0,$$
$$\widetilde{\mathrm{K2}}: \ \left(\tilde{\beta}_{r,n}^{\mathrm{op}}\right)^2 + \left(\tilde{\beta}_{t,n}^{\mathrm{op}}\right)^2 \leq P_{\mathrm{A}}^{\max}, \quad \widetilde{\mathrm{K3}}: \ \tilde{\lambda}_n^{\mathrm{op}} \geq 0,$$
$$\widetilde{\mathrm{K4}}: \ \tilde{\lambda}_n^{\mathrm{op}} \left(\left(\tilde{\beta}_{r,n}^{\mathrm{op}}\right)^2 + \left(\tilde{\beta}_{t,n}^{\mathrm{op}}\right)^2 - P_{\mathrm{A}}^{\max} \right) = 0. \quad (60)$$

Note that in the KKT condition $\widetilde{\mathrm{K1}}$, if $\lambda_n^{\mathrm{op}} = 0$, we have $a_{i,n} = 0$, which violates the condition $a_{i,n} < 0$. Hence, $\lambda_n^{\mathrm{op}} > 0$ holds, which implies that $(\tilde{\beta}_{r,n}^{\mathrm{op}})^2 + (\tilde{\beta}_{t,n}^{\mathrm{op}})^2 - P_{\mathrm{A}}^{\max} = 0$ from the KKT condition $\widetilde{\mathrm{K4}}$. Therefore, we can put $\tilde{\beta}_{r,n}^{\mathrm{op}} = -\frac{a_{r,n}}{2\lambda_n^{\mathrm{op}}}$ and $\tilde{\beta}_{t,n}^{\mathrm{op}} = -\frac{a_{t,n}}{2\lambda_n^{\mathrm{op}}}$ derived from the KKT condition $\widetilde{\mathrm{K1}}$ into $(\tilde{\beta}_{r,n}^{\mathrm{op}})^2 + (\tilde{\beta}_{t,n}^{\mathrm{op}})^2 - P_{\mathrm{A}}^{\max} = 0$, so that

$$\lambda_n^{\mathrm{op}} = \frac{\sqrt{a_{t,n}^2 + a_{r,n}^2}}{2\sqrt{P_{\mathrm{A}}^{\max}}}. \quad (61)$$

Combining $\tilde{\beta}_{r,n}^{\mathrm{op}} = -\frac{a_{r,n}}{2\lambda_n^{\mathrm{op}}}$, $\tilde{\beta}_{t,n}^{\mathrm{op}} = -\frac{a_{t,n}}{2\lambda_n^{\mathrm{op}}}$, and (61) yields $\tilde{\beta}_{r,n} = \varsigma_{r,n}$ and $\tilde{\beta}_{t,n} = \varsigma_{t,n}$.

This completes the proof of **Proposition 2**.

REFERENCES

[1] F. Liu, C. Masouros, A. P. Petropulu, H. Griffiths, and L. Hanzo, "Joint radar and communication design: Applications, state-of-the-art, and the road ahead," *IEEE Trans. Commun.*, vol. 68, no. 6, pp. 3834–3862, Jun. 2020.

[2] F. Liu, L. Zhou, C. Masouros, A. Li, W. Luo, and A. Petropulu, "Toward dual-functional radar-communication systems: Optimal waveform design," *IEEE Trans. Signal Process.*, vol. 66, no. 16, pp. 4264–4279, Aug. 2018.

[3] F. Liu, Y.-F. Liu, A. Li, C. Masouros, and Y. C. Eldar, "Cramér-Rao bound optimization for joint radar-communication beamforming," *IEEE Trans. Signal Process.*, vol. 70, pp. 240–253, 2022.

[4] M. Hua, Q. Wu, C. He, S. Ma, and W. Chen, "Joint active and passive beamforming design for IRS-aided radar-communication," *IEEE Trans. Wireless Commun.*, vol. 22, no. 4, pp. 2278–2294, Apr. 2023.

[5] X. Wang, Z. Fei, J. Guo, Z. Zheng, and B. Li, "RIS-assisted spectrum sharing between MIMO radar and MU-MISO communication systems," *IEEE Wireless Commun. Lett.*, vol. 10, no. 3, pp. 594–598, Mar. 2021.

[6] Z. Esmaeilbeig, A. Eamaz, K. V. Mishra, and M. Soltanalian, "Joint waveform and passive beamformer design in multi-IRS-aided radar," in *Proc. IEEE Int. Conf. Acoust., Speech Signal Process. (ICASSP)*, Jun. 2023, pp. 1–5.

[7] Q. Wu and R. Zhang, "Towards smart and reconfigurable environment: Intelligent reflecting surface aided wireless network," *IEEE Commun. Mag.*, vol. 58, no. 1, pp. 106–112, Jan. 2020.

[8] J. Xu, Y. Liu, X. Mu, R. Schober, and H. V. Poor, "STAR-RISs: A correlated T&R phase-shift model and practical phase-shift configuration strategies," *IEEE J. Sel. Topics Signal Process.*, vol. 16, no. 5, pp. 1097–1111, Aug. 2022.

[9] X. Mu, Y. Liu, L. Guo, J. Lin, and R. Schober, "Simultaneously transmitting and reflecting (STAR) RIS aided wireless communications," *IEEE Trans. Wireless Commun.*, vol. 21, no. 5, pp. 3083–3098, May 2022.

[10] Z. Wang, X. Mu, and Y. Liu, "STARS enabled integrated sensing and communications," *IEEE Trans. Wireless Commun.*, vol. 22, no. 10, pp. 6750–6765, Oct. 2023.

[11] Z. Zhang, Y. Liu, Z. Wang, and J. Chen, "STARS-ISAC: How many sensors do we need?," *IEEE Trans. Wireless Commun.*, vol. 23, no. 2, pp. 1085–1099, Feb. 2024.

[12] W. Wei, X. Pang, C. Xing, N. Zhao, and D. Niyato, "STAR-RIS aided secure NOMA integrated sensing and communication," *IEEE Trans. Wireless Commun.*, vol. 23, no. 9, pp. 10712–10725, Sep. 2024.

[13] J. Xu, J. Zuo, J. T. Zhou, and Y. Liu, "Active simultaneously transmitting and reflecting (STAR)-RISs: Modeling and analysis," *IEEE Commun. Lett.*, vol. 27, no. 9, pp. 2466–2470, Sep. 2023.

[14] Z. Zhang et al., "Active RIS vs. passive RIS: Which will prevail in 6G?," *IEEE Trans. Commun.*, vol. 71, no. 3, pp. 1707–1725, Mar. 2023.

[15] S. Zhang et al., "Joint beamforming optimization for active STAR-RIS-assisted ISAC systems," *IEEE Trans. Wireless Commun.*, vol. 23, no. 11, pp. 15888–15902, Nov. 2024.

[16] D. Han et al., "Multi-functional RIS integrated sensing and communications for 6G networks," *IEEE Trans. Wireless Commun.*, vol. 24, no. 2, pp. 1146–1161, Feb. 2025.

[17] Q. Zhu, M. Li, R. Liu, and Q. Liu, "Cramér-rao bound optimization for active RIS-empowered ISAC systems," *IEEE Trans. Wireless Commun.*, vol. 23, no. 9, pp. 11723–11736, Sep. 2024.

[18] C. Wu, C. You, Y. Liu, X. Gu, and Y. Cai, "Channel estimation for STAR-RIS-aided wireless communication," *IEEE Commun. Lett.*, vol. 26, no. 3, pp. 652–656, Mar. 2022.

[19] L. Yu et al., "Channel estimation for STAR-RIS-aided communications based on deep iterative networks," in *Proc. 3rd Int. Conf. Intell. Commun. Comput. (ICC)*, 2023, pp. 119–123.

[20] X. Liu, T. Huang, N. Shlezinger, Y. Liu, J. Zhou, and Y. C. Eldar, "Joint transmit beamforming for multiuser MIMO communications and MIMO radar," *IEEE Trans. Signal Process.*, vol. 68, pp. 3929–3944, 2020.

[21] N. L. Tsitsas and C. Valagiannopoulos, "Anomalous refraction into free space with all-dielectric binary metagratings," *Phys. Rev. Res.*, vol. 2, Sep. 2020, Art. no. 033526, doi: 10.1103/PhysRevResearch.2.033526.

[22] T. He et al., "Perfect anomalous refraction metasurfaces empowered half-space optical beam scanning," *Nature Commun.*, vol. 16, no. 1, p. 3115, Apr. 2025.

[23] B. Elmaroud, "Spectral efficiency analysis and optimization in hybrid RIS systems under nonlinear power amplifier effects," *Wireless Pers. Commun.*, vol. 144, nos. 3–4, pp. 553–575, Oct. 2025. [Online]. Available: https://api.semanticscholar.org/CorpusID:282660758

[24] N. Kolomvakis, A. Kosasih, and E. Björnson, "Nonlinear distortion radiated from large arrays and active reconfigurable intelligent surfaces," *IEEE Trans. Wireless Commun.*, vol. 24, no. 6, pp. 5037–5049, Jun. 2025.

[25] R. Long, Y.-C. Liang, Y. Pei, and E. G. Larsson, "Active reconfigurable intelligent surface-aided wireless communications," *IEEE Trans. Wireless Commun.*, vol. 20, no. 8, pp. 4962–4975, Aug. 2021.

[26] M. Di Renzo et al., "Reconfigurable intelligent surfaces vs. Relaying: Differences, similarities, and performance comparison," *IEEE Open J. Commun. Soc.*, vol. 1, pp. 798–807, 2020.

[27] X. Song, J. Xu, F. Liu, T. X. Han, and Y. C. Eldar, "Intelligent reflecting surface enabled sensing: Cramér-Rao bound optimization," *IEEE Trans. Signal Process.*, vol. 71, pp. 2011–2026, 2023.

[28] X. Shao, C. You, W. Ma, X. Chen, and R. Zhang, "Target sensing with intelligent reflecting surface: Architecture and performance," *IEEE J. Sel. Areas Commun.*, vol. 40, no. 7, pp. 2070–2084, Jul. 2022.

[29] C. Xu and S. Zhang, "MIMO integrated sensing and communication exploiting prior information," *IEEE J. Sel. Areas Commun.*, vol. 42, no. 9, pp. 2306–2321, Sep. 2024.

[30] S. M. Kay, *Fundamentals Of Statistical Signal Processing: Estimation Theory*. Upper Saddle River, NJ, USA: Prentice-Hall, 1993.

[31] T.-T. Lu and S.-H. Shiou, "Inverses of 2×2 block matrices," *Comput. Math. Appl.*, vol. 43, no. 1, pp. 119–129, 2002. [Online]. Available: https://www.sciencedirect.com/science/article/pii/S0898122101002784

[32] Q. Shi and M. Hong, "Penalty dual decomposition method for nonsmooth nonconvex optimization—Part I: Algorithms and convergence analysis," *IEEE Trans. Signal Process.*, vol. 68, pp. 4108–4122, 2020.

[33] M. Grant and S. Boyd. (Mar. 2014). *CVX: MATLAB Software for Disciplined Convex Programming, Version 2.1*. [Online]. Available: https://cvxr.com/cvx

[34] Q. Wu and R. Zhang, "Intelligent reflecting surface enhanced wireless network: Joint active and passive beamforming design," in *Proc. IEEE Global Commun. Conf. (GLOBECOM)*, Dec. 2018, pp. 1–6.

[35] G. Zhou, C. Pan, H. Ren, K. Wang, M. D. Renzo, and A. Nallanathan, "Robust beamforming design for intelligent reflecting surface aided MISO communication systems," *IEEE Wireless Commun. Lett.*, vol. 9, no. 10, pp. 1658–1662, Oct. 2020.

[36] M. Hua, Q. Wu, W. Chen, O. A. Dobre, and A. L. Swindlehurst, "Secure intelligent reflecting surface-aided integrated sensing and communication," *IEEE Trans. Wireless Commun.*, vol. 23, no. 1, pp. 575–591, Jan. 2024.

[37] R. Ma, Y. Peng, R. Ye, M. Yue, F. Al-Hazemi, and J. Lee, "Active RIS-assisted secure communications against simultaneous jamming and eavesdropping," *IEEE Wireless Commun. Lett.*, vol. 14, no. 3, pp. 686–690, Mar. 2025.

[38] W. Wang, W. Ni, H. Tian, Y. C. Eldar, and R. Zhang, "Multi-functional reconfigurable intelligent surface: System modeling and performance optimization," *IEEE Trans. Wireless Commun.*, vol. 23, no. 4, pp. 3025–3041, Apr. 2024.

[39] H. Jia, X. Li, and L. Ma, "Physical layer security optimization with Cramér–Rao bound metric in ISAC systems under sensing-specific imperfect CSI model," *IEEE Trans. Veh. Technol.*, vol. 73, no. 5, pp. 6980–6992, May 2024.

[40] Z. Peng, Z. Zhang, C. Pan, M. D. Renzo, O. A. Dobre, and J. Wang, "Beamforming optimization for active RIS-aided multiuser communications with hardware impairments," *IEEE Trans. Wireless Commun.*, vol. 23, no. 8, pp. 9884–9898, Aug. 2024.

[41] S. Qin et al., "Multifunctional topological metasurfaces with modular Meta-atoms for multidimensional wave control," *Adv. Opt. Mater.*, vol. 13, no. 14, May 2025, Art. no. 2500044.

[42] S. A. Hassani Gangaraj, C. Valagiannopoulos, and F. Monticone, "Topological scattering resonances at ultralow frequencies," *Phys. Rev. Res.*, vol. 2, no. 2, 2020, Art. no. 023180.

[43] S. P. Boyd and L. Vandenberghe, *Convex Optimization*. Cambridge, U.K.: Cambridge Univ. Press, 2004.

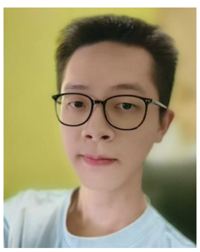

Runlong Ye (Graduate Student Member, IEEE) received the M.S. and Ph.D. degrees in communication engineering and electronic information technology from Macau University of Science and Technology (MUST) in 2022 and 2025, respectively. He is currently a Theoretical Instructor with the Civil Aircraft Intelligent Maintenance Research Center and 147 maintenance training base at Guangzhou Civil Aviation College (GCAC), Guangzhou, China. His research interests include physical layer security, RIS-assisted communications, and integration of sensing and communications.

Yuyang Peng (Senior Member, IEEE) received the M.S. and Ph.D. degrees in electrical and electronic engineering from Chonbuk National University, Jeonju, South Korea, in 2011 and 2014, respectively. He was a Post-Doctoral Research Fellow with Korea Advanced Institute of Science and Technology (KAIST), Daejeon, South Korea, from 2014 to 2018. He is currently an Associate Professor with the School of Computer Science and Engineering, Macau University of Science and Technology (MUST), Taipa, Macau. His research activities lie in the broad area of digital communications, wireless sensor networks, and computing. In particular, his current research interests include cooperative communications, spatial modulation, and communication security. He served as an Editor for IEEE ACCESS.

Ming Yue received the B.S., M.S., and Ph.D. degrees in electronic and information engineering, communication engineering, and electronic information technology from Macau University of Science and Technology (MUST), Taipa, Macau in 2021, 2023, and 2026, respectively. His research interests include spatial modulation, RIS aided communications, antenna selection, and the Internet of Things (IoT).

Wei Gan received the B.E. degree in electrical engineering and automation and the M.S. degree in control theory and control engineering from Wuhan University of Technology (WUT), Wuhan, China, and the Ph.D. degree in electronic information technology, Macau University of Science and Technology (MUST), Macau, China, in 2026. Her current research interests include RIS-assisted communications, physical layer security, and wireless information and power transfer.

Fawaz AL-Hazemi (Senior Member, IEEE) received the B.S. degree in computer engineering from the King Fahd University of Petroleum and Minerals (KFUPM), Dhahran, Saudi Arabia, in 2003, and the M.S. and Ph.D. degrees from Korea Advanced Institute of Science and Technology (KAIST), Daejeon, South Korea, in 2010 and 2019, respectively. He is currently an Assistant Professor with the College of Computer Science and Engineering, University of Jeddah, Saudi Arabia, where he is the Deputy Supervisor of the Digital Transformation and Information Technology (IT) Center. His research interests are green data center, energy-aware computing, and communications.

Juho Lee (Fellow, IEEE) received the B.S., M.S., and Ph.D. degrees in electrical engineering from Korea Advanced Institute of Science and Technology (KAIST), South Korea, in 1993, 1995, and 2000, respectively. In 2000, he joined Samsung Electronics and he was with multiple generations of mobile communications, such as WCDMA and HSDPA in 3G, LTE, LTE-Advanced, and LTE-Advanced Pro in 4G, and 5G NR technologies. He is currently a fellow (EVP of technology) with Samsung Electronics, where he is currently on research and standardization for mobile communications. His current research interests include the preparation of future technologies, such as 5G evolution, e.g., 5G-advanced in 3GPP and 6G. He was the Vice Chair of 3GPP RAN WG1 from February 2003 to August 2009 and chaired LTE/LTE-Advanced MIMO sessions. He also served as the rapporteur of the work item for specifying CoMP in 3GPP LTE-Advanced Rel-11. He serves as the Guest Editor for *IEEE Communications Standards Magazine*.

Raouf Boutaba (Fellow, IEEE) received the M.Sc. and Ph.D. degrees in computer science from Sorbonne University in 1990 and 1994, respectively. He is currently a University Chair Professor and the Director of the David R. Cheriton School of Computer Science, University of Waterloo, Canada. His research interests include computer networking and distributed systems. He served as the founding Editor-in-Chief of IEEE TRANSACTIONS ON NETWORK AND SERVICE MANAGEMENT from 2007 to 2010 and the Editor-in-Chief for IEEE JOURNAL ON SELECTED AREAS IN COMMUNICATIONS from 2018 to 2021. He is a fellow of the Engineering Institute of Canada, the Canadian Academy of Engineering, and the Royal Society of Canada.